Earth and Space Science

RESEARCH ARTICLE
10.1029/2023EA002938

Modeling Wavelength Dependent Mid-Infrared (5.5–25 μm) Optical Constants of Silicate Glasses: A Genetic Algorithm Approach

I. Varatharajan[1], E. Sklute[2,3], T. D. Glotch[1], and M. D. Dyar[2,4]

[1]Department of Geosciences, Stony Brook University, Stony Brook, NY, USA, [2]Planetary Science Institute, Tucson, AZ, USA, [3]Los Alamos National Laboratory, Los Alamos, NM, USA, [4]Department of Astronomy, Mount Holyoke College, South Hadley, MA, USA

Key Points:

- MIR optical constants (5.56–25 μm; 400–1,800 cm^{-1}) and their oscillator parameters were modeled for seven silicate glasses of varying SiO_2 wt%
- MicroFTIR reflectance spectra of the glasses studied were measured for the spectral region 5.56–25 μm (400–1,800 cm^{-1})
- Genetic algorithm was adopted to automatically find the natural oscillators and their parameters for the glasses studied

Correspondence to:

I. Varatharajan,
indhu.varatharajan@stonyrbrook.edu

Citation:

Varatharajan, I., Sklute, E., Glotch, T. D., & Dyar, M. D. (2023). Modeling wavelength dependent mid-infrared (5.5–25 μm) optical constants of silicate glasses: A genetic algorithm approach. *Earth and Space Science*, *10*, e2023EA002938. https://doi.org/10.1029/2023EA002938

Received 14 MAR 2023
Accepted 16 AUG 2023

Author Contributions:

Conceptualization: I. Varatharajan, E. Sklute, T. D. Glotch, M. D. Dyar
Data curation: I. Varatharajan, T. D. Glotch, M. D. Dyar
Formal analysis: I. Varatharajan
Funding acquisition: E. Sklute, T. D. Glotch, M. D. Dyar
Investigation: I. Varatharajan, E. Sklute
Methodology: I. Varatharajan, E. Sklute, T. D. Glotch, M. D. Dyar
Project Administration: E. Sklute, T. D. Glotch, M. D. Dyar
Resources: I. Varatharajan, E. Sklute, T. D. Glotch, M. D. Dyar
Software: I. Varatharajan, E. Sklute, T. D. Glotch, M. D. Dyar
Supervision: E. Sklute, T. D. Glotch, M. D. Dyar

Abstract Wavelength-dependent mid-infrared (400–1,800 cm^{-1}; 5.56–25 μm) optical constants (real and imaginary indices of refraction; *n* and *k*) are determined using reflectance spectra at a spectral sampling of 4 cm^{-1} for several silicate glasses of varying SiO_2 wt% which include (a) basaltic volcanic glass from Kīlauea, Hawaii, (b) synthetic andesite, (c) two synthetic dacites, (d) obsidian volcanic glass from Mount Lassen, California, (e) synthetic rhyodacite, and (f) rhyolitic volcanic glass from Mexico. Because glasses are optically isotropic, no specific orientation was required for spectral measurements, and polished glass samples were measured at random orientations using micro-FTIR spectrometer. Lorentz-Lorenz dispersion theory and Fresnel reflectance model for high symmetry materials were used to model the optical constants by optimizing oscillator parameters in modeled spectra to match laboratory spectra. A genetic algorithm (GA) approach automatically finds the natural oscillators and their parameters for each spectrum, and then uses these parameters in a non-linear least squares optimization routine. The study compared spectral parameters such as Christiansen feature, reststrahlen bands (RBs), and the peaks centered around 860–1,100 (peak 1) and 400–480 cm^{-1} (peak 2) of *n* and *k* to their respective SiO_2 wt% of the glasses. CF, RBs, peak 1 of *n* and *k*, and peak 2 of *n* shift to higher wavenumbers with increased SiO_2 wt%, whereas peak 2 of *k* shifts to lower wavenumbers with increased SiO_2 wt%. Derived optical constants of these glasses will improve quantitative abundance mapping of volcanic materials on the surfaces of silicate targets in the Solar System.

Plain Language Summary The effective mapping of minerals and their abundances on a planet's surface from orbit is enabled by understanding the nature of the interaction of light of varying wavelengths with the planetary surface. The reflected/emitted light from the surface directly depends on the optical properties of the materials and their interaction with each other. In this study, we numerically modeled the mid-infrared optical constants of silicate glasses using a genetic algorithm (GA) approach. The GA allows the model to automatically locate the natural harmonic oscillators and their parameters that are responsible for creating the spectral signals that can be detected by spectrometers on orbital spacecraft. Derived optical constants of the glasses could be used in radiative transfer models for quantitative mineral mapping applications. Glasses on planetary surfaces are common in volcanic and/or impact materials and the mid-infrared spectral range has been widely used to map the surface mineralogy of planets including the Moon and Mars. Mapping the composition and abundance of these glasses therefore will help us to understand the thermal evolution of the planets themselves.

1. Introduction

Silicate glasses are abundant in the regoliths of various rocky planets in our solar system such as the Earth, Moon, Mars, Mercury, and large asteroids. Silicate glasses are super-cooled liquids with a poorly ordered internal structures comprised of loosely linked SiO_4 tetrahedra containing a significant amount of intermolecular space (Fisher & Schmincke, 1984). Glasses broadly originate from either volcanic (Saal et al., 2008; Wilson & Head, 1981) or hypervelocity impact processes (Stöffler, 1984; Tompkins & Pieters, 2010). Glasses are formed when molten material (volcanic magma or impact melts) rapidly cools below the glass transition temperature (Fisher & Schmincke, 2012; Stöffler, 1984). Volcanic processes play a major role in shaping the geology and composition of the surfaces of the terrestrial planets including Earth (Patrick & Howe, 1994), the Moon (Bhattacharya et al., 2013; Haruyama et al., 2009; Head & Wilson, 1992; Pieters et al., 2001; Schultz & Spudis, 1983), Mars

Validation: I. Varatharajan
Visualization: I. Varatharajan
Writing – original draft: I. Varatharajan
Writing – review & editing: I. Varatharajan, E. Sklute, T. D. Glotch, M. D. Dyar

(Brož et al., 2021; Garvin et al., 2000; Hauber et al., 2011; McEwen et al., 1999; Zimbelman et al., 2015), Venus (D'Incecco et al., 2022; Herrick & Hensley, 2023; Ivanov et al., 2015; Nimmo & McKenzie, 1998; Smrekar et al., 2010), and Mercury (Besse et al., 2015; Jozwiak et al., 2018; Kerber et al., 2009, 2011; Thomas et al., 2014; Weider et al., 2016).

Remote compositional mapping of volcanic materials and their abundances and physical characteristics gives clues to the source of melting, type of eruption (effusive or explosive), nature and abundance of volatiles in the planetary interior, and thermal history of the planet itself (Elkins-Tanton et al., 2007; Head et al., 2009; Kerber et al., 2009; Saal et al., 2013). Volcanic glass compositions hold clues to primary melt compositions and their volatile species (Saal et al., 2008). Thus, characterizing their compositions and abundances is a crucial step in understanding the chemical compositions of planetary surfaces that, in turn, can project an understanding into their interiors and their thermal evolution. Impact glasses, by comparison, are formed by the high temperatures and pressures generated during an impact event, such as a meteor or asteroid impacts (Chao, 1967). The composition of impact glass can vary depending on the composition of the target material and the impactor (Zellner, 2019). Typically, impact glass contains a mixture of the target material and impactor material, along with some vapourized material that has condensed to form glass (Dressler & Reimold, 2001). The exact composition of the impact glass can provide information about the temperature, pressure, and duration of the impact event (Dressler & Reimold, 2001). Therefore, the study of impact glass can provide important insights into the geological history of planetary surfaces, the types of materials that have been present on these surfaces over time, and the nature of impact events that have shaped these surfaces (Long et al., 2022). For both types of glasses (volcanic and impact), understanding the composition, distribution, and abundance is integral to interpreting planetary evolution.

Remote sensing is the predominant method for examining the compositions of planetary surfaces, and it relies on the knowledge of the physical properties of surface materials. Spectral signatures of the minerals are well-studied and are fairly diagnostic from orbital datasets, but those of glasses are more difficult to interpret due to their lack of fine vibrational spectral bands (Fu et al., 2017; Speck et al., 2011). Identifying the compositions and abundances of these glasses on planetary surfaces can be a uniquely challenging task that hinges on the breadth of the spectral library of analog materials and the models used to apply them to planetary data. Decades of MIR spectral data have been collected by orbiters around the Moon and Mars. The Diviner Lunar Radiometer Experiment onboard Lunar Reconnaissance Orbiter has been collecting global thermal emission data of the Moon in multiple spectral channels since 2009 (Paige et al., 2010). The Thermal Emission Imaging System onboard Mars Odyssey has been collecting wavelength dependent multispectral thermal emission images of the Martian surface for over two decades since its orbit insertion in 2001 (Christensen et al., 2004a) and the Thermal Emission Spectrometer (TES) onboard Mars Global Surveyor collected hyperspectral MIR spectra of Mars for 10 years between 1996 and 2006 (Christensen et al., 2001). The Planetary Fourier Spectrometer onboard Mars Express is optimized to study the thermal emission of the planet in the infrared spectral range of 1.2–45 μm and has been providing the spectral data since 2003 (Formisano et al., 2005). Furthermore, the miniTES (Miniature TES) instruments (a miniaturized version of MGS-TES) onboard the Mars Exploration Rovers Spirit (2004–2011) and Opportunity (2004–2018) have collected thermal emission spectra for over a decade of multiple target surfaces in hyperspectral mode with the highest spatial resolution of 8 mrad and capable of characterizing the sample size of 8 cm (Christensen et al., 2003, 2004b; Silverman et al., 2006). Previous studies have investigated the MIR spectral behavior of a variety of glasses to support their detection from the orbit, which include glasses within tephra deposits (Leight et al., 2022), synthetic glasses of varying fugacity, bulk chemistry, and temperatures (Cannon et al., 2017), synthetic glasses analogous to materials on Mars (Minitti & Hamilton, 2010; Moroz et al., 2009) and Mercury (Morlok et al., 2021), volatiles within glasses (King & Larsen, 2013), synthetic basaltic glasses with varying SiO_2, FeO content, Fe^{3+}/Fe^{2+}, and alkali elements (Dufresne et al., 2009), ternary glasses (Mocioiu et al., 2013), quartzofeldspathic glasses (Byrnes et al., 2007), and feldspathic and impact glass (Jaret et al., 2015, 2018; Johnson et al., 2020).

While spectral data exist for many glass compositions, the glasses on planetary surfaces are most likely present in the form of fine particulates as volcanic ash or fine-grained regolith (Pieters et al., 1993; Tompkins & Pieters, 2010). Even at MIR wavelengths, spectral mixing is nonlinear for these fine particulates and radiative transfer theory is required to extract the quantitative abundances of these glasses and other phases present (Arnold, 2014; Hamilton et al., 2021). However, radiative transfer theory requires the optical constants (the real (n) and imaginary (k) parts of the complex refractive index) of each material in a mixture. These quantities, which vary with wavelength, are critical inputs to radiative transfer theory models that depend on the fundamental structural and chemical properties of the materials present in a mixture, and which account for the non-linearity of spectral mixing when light interacts with more than one phase before being reflected to the detector (Ito et al., 2017; Toon et al., 1977). Despite their importance in spectral modeling, optical constants of glasses over many planetary relevant compositions and instrument-relevant wavelength ranges are still lacking from the literature, limiting our ability to correctly interpret the afore-mentioned volcanic processes through remote observations.

To begin to fill this gap, this study derives MIR optical constants of four planetary-relevant synthetic glass compositions: andesite "lava," rhyodacite, and two dacites, along with three natural samples: basaltic volcanic glass from Hawaii, rhyolitic volcanic glass from Mexico, and obsidian volcanic glass from Lassen, California. Because the glasses are optically isotropic, Lorentz-Lorenz dispersion theory and a Fresnel reflectance model for isotropic materials are used to model the optical constants as a function of wavelength between 400 and 1,800 cm^{-1} (5.56–25 μm) with a spectral sampling of 4 cm^{-1} using the envelope of the measured reflectance spectrum of the glasses at normal incidence.

This study improves on previous Lorentz-Lorenz based models (Aronson & Strong, 1975; Spitzer & Kleinman, 1961) with the implementation of a genetic algorithm (GA). GAs are a heuristic approach inspired by the process of natural selection in biological evolution (Fraser, 1957; Holland, 1992). Biological evolution occurs through the gradual change in the genetic makeup of populations over successive generations. It is driven by mechanisms such as mutation, recombination/crossover, and selection. Mutations introduce genetic variation, recombination shuffles and combines genetic information, and selection favors individuals with advantageous traits, leading to their increased representation in subsequent generations. GAs mimic these principles to solve optimization problems in computational systems. They involve encoding potential solutions as chromosomes or strings of genes (representing parameters or characteristics) and iteratively applying operations similar to mutation and crossover to generate new solutions. The fitness of each solution is evaluated based on its performance in solving the problem, and selection mechanisms determine which solutions are more likely to contribute to the next generation. By iterating this process over multiple generations, GAs explore and exploit the solution space, converging toward increasingly better solutions. The principles of selection, variation, and heredity in GAs parallel the mechanisms of natural selection, genetic variation, and inheritance in biological evolution. GAs effectively leverage the concepts of genetic diversity, reproduction, and selection pressure to evolve and improve solutions to complex problems, just as natural selection shapes and refines organisms in response to environmental challenges. While GAs are a simplified computational abstraction of biological evolution, they provide a powerful approach for optimization and problem-solving in various domains, drawing inspiration from the successful adaptive processes observed in nature. GAs are widely used in optimization, machine learning, and artificial intelligence (Grefenstette, 1993; Tomassini, 1995). They are particularly useful in problems where the search space is very large and the objective function is complex, non-linear, or noisy, such as spectral signatures. GAs have been successfully demonstrated for computing optical constants by previous studies (Djurišić et al., 1997a; Güngör & Saka, 2004; Torres-Costa et al., 2004).

This study uses a GA to automatically find the natural oscillators that are responsible for the spectral features in the measured reflectance spectra of the glasses, and to optimize the frequencies (ν), damping coefficient (γ), band strength ($4\pi\rho$), and dielectric constant (ε_0) of the oscillators. Oscillator frequencies and parameters found by the GA are further fine-tuned using a pre-existing nonlinear least squares optimization routine (LSQ). Without the GA-routine, the initial guesses of the number of oscillators and its parameters (ν_j, $4\pi\rho_j$, γ_j) and ε_0 are assigned manually, a subjective step that can significantly affect the modeled optical constants. This study presents both derived optical constants and the new methodology used for their derivation. Unlike spectral reflectance measurements that vary with viewing conditions, grain size, and surface roughness, the optical constants are fundamental bulk properties of any given mineral that depend on only on its composition and crystal structure. The nature of the measured reflectance and modeled optical constants as a function of $\mathrm{SiO_2}$ wt% as an indicator of chemical composition are further discussed in Section 4. This database of MIR optical constants of glasses will enable more quantitative MIR spectroscopic analysis of fine particulate surfaces of volcanic complexes of solar system objects.

2. Samples

Volcanic glasses used in this study were obtained from collections at Mount Holyoke College and were donated by Jennifer Blank. The chemical characterization of the volcanic glasses is listed in Table 1. The four synthetic

Table 1
Chemical Compositions of the Glasses Studied

	Andesite synthetic	Dacite 1 syntnetic	Dacite 2 synthetic	Rhyodacite synthetic	Rhyolite Mexico natural	Basalt Kilauea, Hawaii natural	Obsidian Lassen, CA natural
Sample number	82–70	85–3	83–59	85–43	–	–	–
P_2O_5	0.12	0.76	0.14	0.10	0.01	0.24	0.02
SiO_2	58.81	66.47	67.07	74.94	75.89	49.62	74.61
SO_2	0.00	0.00	0.00	0.00	0.00	0.03	0.01
TiO_2	0.71	0.74	0.54	0.29	0.15	2.67	0.15
Al_2O_3	17.07	18.01	17.67	15.80	11.35	12.85	12.80
Cr_2O_3	0.00	0.03	0.03	0.00			
MgO	6.24	0.06	2.48	0.45	0.01	6.23	0.14
CaO	7.83	4.24	5.02	1.81	0.16	10.61	0.76
MnO	0.12	2.52	0.40	0.02	0.09	0.18	0.04
FeO (total)	5.85	0.86	2.73	1.67	2.62	11.61	0.98
Na_2O	2.14	3.57	2.77	2.57	5.13	2.39	3.68
K_2O	0.28	1.72	0.65	1.29	4.14	0.46	4.77
F	0.00	0.00	0.00	0.00	0.00	0.00	0.00
Cl		0.37	0.40	0.20			
Total	99.17	99.35	99.89	99.14	99.55	96.89	97.96
$\%Fe^{3+}$	53	59	0	35	35	16	21
FeO Mössbauer	2.75	0.35	2.73	1.09	1.70	9.75	0.77
Fe_2O_3 Mössbauer	3.45	0.56	0.00	0.65	1.02	2.06	0.23
Revised total	99.52	99.41	99.89	99.20	99.65	97.10	97.98

samples were made for MDD at Corning Glass ca. 1986 and chosen to model potential lunar compositions. The natural basalt sample was collected by Tim Orr (USGS, HVO) from Kilauea. The Lassen glass is a blue obsidian from Lassen, CA. The Mexico glass does not have providence information but is likely from the Tequila volcano. All synthetic glasses, along with the Lassen blue obsidian, were chemically characterized using electron probe microanalysis at Brown University (Joseph Boesenberg, analyst). Synthetic glasses were analyzed using a rhyolitic glass set-up, with calibration tested on a rhyolite standard (VG568). The Hawaiian basaltic glass and Mexico volcanic glass were analyzed for major elements using X-ray Fluorescence (XRF) in the laboratory of Dr. J. Michael Rhodes at the University of Massachusetts (Rhodes & Vollinger, 2004) using his standard protocols (Dyar et al., 2019). Values for FeO (total) given in Table 1 come from the techniques used above for all the major elements; Fe_2O_3 (total) values from XRF have been converted to FeO (total). Mössbauer spectroscopy was used to determine the Fe^{3+} and Fe^{2+} contents of all glasses following the methodology of Dyar et al. (2016) and those ratios were used to convert total FeO to Fe_2O_3 and FeO (cf. Dyar et al. (2008)).

3. Methods

3.1. MIR Spectroscopy of the Glasses

Because glasses are optically isotropic, their optical constants can be obtained from a randomly selected fragment, polished along any direction. For this study, glass fragments (of at least ~0.5 cm in width and thickness) were mounted onto a slide, and the exposed top surface was polished until it was leveled and smooth, with a roughness of ≤1 μm. This was achieved by using polishing paper with decreasing abrasiveness, ranging from 50 to 1 μm roughness. Micro-FTIR spectra of the polished glasses were then collected using a Nicolet iN10MX FTIR microscope with a deuterated triglycine sulfate detector in the Center for Planetary Exploration at Stony Brook University. Point spectra covering 400–1,800 cm^{-1} (5.56–25 μm) with a spectral sampling of 4 cm^{-1} were collected with a 300 × 300 μm spot size for at least three different spots of the same sample, where each single 300 × 300 μm spot spectrum is an average of 1,024 scans. Sample spectra were referenced to a gold mirror using the same spot size and number of scans as samples; a reference was taken before each sample measurement. The averaged microFTIR spectrum of three different spots for each glass sample was slightly noisy. Therefore, this averaged spectrum is further smoothed using a Savitzky-Golay filter (Schafer, 2011).

3.2. Modeling Optical Constants: Theory and Implementation

The wavelength-dependent optical constants of a material can be modeled by comparing the measured known laboratory spectra of a material against the reflectance spectra modeled by combining the mathematical expressions of classical dispersion theory (Aronson & Strong, 1975; Glotch et al., 2007; Mooney & Knacke, 1985; Onari et al., 1977; Pollack et al., 1973; Querry et al., 1978; Roush et al., 1991; Spitzer & Kleinman, 1961) and a Fresnel reflectance model at normal incidence (Hansen & Travis, 1974).

When infrared light interacts with a mineral, each vibrational mode in a material creates a moving dipole moment that, in turn, produces radiation. This radiation is measured as the resulting infrared spectrum of that mineral. The mathematical relation between the total vibration of a mineral and the sum of two or more individual harmonic oscillators is given by classical Lorentz-Lorenz dispersion theory. Each model harmonic oscillator is defined by three oscillation parameters: the center of frequency of the oscillation (ν), band strength ($4\pi\rho$), and damping coefficient (γ). An additional non-oscillator dependent term is the high-frequency dielectric constant (ε_0), which is a bulk-mineral property. The ε_0 is roughly equal to $n_{\text{vis}}{}^2$ measured in the visible part of the spectrum (Roush et al., 1991). In this study, the Spitzer and Kleinman (1961) formulation of the classical dispersion theory is adopted, expressed in wavenumber space. The relation between the optical constants (n and k) and the dispersion parameters is given as:

$$n^2 - k^2 = \varepsilon_0 + \sum_j \frac{4\pi\rho_j \nu_j^2 \left(\nu_j^2 - \nu^2\right)}{\left(\nu_j^2 - \nu^2\right)^2 + \left(\gamma_j^2 \nu_j^2 \nu^2\right)} \tag{1}$$

$$nk = \sum_j \frac{2\pi\rho_j \nu_j^2 (\gamma_j \nu_j \nu)}{\left(\nu_j^2 - \nu^2\right)^2 + \left(\gamma_j^2 \nu_j^2 \nu^2\right)}, \tag{2}$$

where the summation is over the lattice oscillators and each (jth) oscillator is described by its strength (ρ_j), damping coefficient (γ_j), and frequency (ν_j) (Spitzer & Kleinman, 1961).

The Fresnel equation relates the reflectivity of the mineral and its optical constants (Spitzer & Kleinman, 1961). The reflectivity of a mineral at normal incidence is mathematically expressed as:

$$\mathrm{R} = \frac{(n-1)^2 + k^2}{(n+1)^2 + k^2} \tag{3}$$

Generally, the modeled reflectance spectrum is produced by first giving ν_j, $4\pi\rho_j$, γ_j, and ε_0 values as input parameters to the dispersion equations (Equations 1 and 2) to solve for n and k, which are then used as inputs into the Fresnel equations for normal incidence (Equation 3). The objective is to find the minimum number of oscillators and the optimum parameters (ν_j, $4\pi\rho_j$, γ_j) and ε_0 of each silicate glass that results in the smallest chi-square value (χ^2) between the modeled and measured reflectance spectrum of each glass.

The major challenge in modeling the optical constants is arriving at the optimum values for the oscillator parameters (ν_j, $4\pi\rho_j$, γ_j) and ε_0 that provide best fit to the measured spectrum. Previous studies (Arnold et al., 2014; Glotch & Rossman, 2009; Glotch et al., 2007; Roush et al., 1991; Rucks et al., 2022; Ye et al., 2019) have used a nonlinear least-square optimization routine (LSQ) that iteratively fits the modeled spectrum produced using Equations 1–3. However, LSQ requires a set of best initial guesses that includes the number of oscillators and their parameters. This has been achieved by an iterative manual trial and error approach in which the guessed parameter values evolve through multiple iterations of the algorithm. As such, the resulting optimized parameters are biased by the initial assumptions made by the user and the breadth of their trial-and-error search space. In this study, this challenge is overcome by utilizing the machine learning "genetic algorithm" (GA) to automatically pick the natural oscillators and calculate their oscillator parameters. These GA-modeled oscillator parameters are then used in the LSQ method to find the best fit for the given reference reflectance spectrum. This enables automated refining of the optimal solutions of the parameters that in turn are used to calculate the n and k values using Equations 1–3. The detailed implementation of the GA-LSQ algorithm is discussion in Section 3.3 below.

3.3. Genetic Algorithm Implementation

Optimization methods are generally classified as local or global search techniques; the solutions produced by the local techniques (such as LSQ) are highly dependent on the starting point (initial conditions), whereas the solutions by global methods (such as GA) are largely independent of the initial conditions. GA is a search and optimization technique that is inspired by the process of natural selection and genetics (Fraser, 1957; Holland, 1992). It is a heuristic approach that is used to solve complex problems by mimicking the process of natural evolution, where the fittest individuals (or chromosomes) are more likely to survive and reproduce. Each chromosome is an array of "genes" that are the basic building blocks of the GA. The GA involves creating a population of potential solutions to a problem, and then applying genetic operators such as crossover, mutation, and selection to evolve the population over multiple generations. Each individual in the population represents a potential solution to the problem, and the fitness of each individual is determined by an objective function that measures how well it solves the problem. During each generation, the individuals in the population are evaluated based on their fitness, and a selection process is used to choose the fittest individuals to be parents for the next generation. These parents then undergo genetic operations such as crossover and mutation to create new offspring that inherit traits from their parents. The process is repeated over many generations, with the hope that the population will evolve to contain individuals that are increasingly fit solutions to the problem.

In our study, the genes represented in the GA are the oscillator parameters and ε_0. Therefore, each chromosome (array of genes) is a $j \times 4$ matrix of possible solutions for ν_j, $4\pi\rho_j$, γ_j, ε_0 for j number of oscillators. The fitness of each chromosome is determined by maximizing the cost function:

$$\chi^2 = \sum_{\nu=400}^{1800} \frac{\left(R_\nu^{\text{modeled}} - R_\nu^{\text{measured}}\right)^2}{R_\nu^{\text{measured}}} \tag{4}$$

$$\text{Fitness}(\nu, 4\pi\rho, \gamma, \varepsilon_0) = \left(1 - \chi^2\right) * 100 \tag{5}$$

where R^{modeled} is the obtained or modeled spectrum from Equations 1–3 and R^{measured} is the desired or measured spectrum. In this optimization procedure, the data is fit wavenumber by wavenumber for every wavenumber (ν) in the spectral range of 400–1,800 cm^{-1}, with intervals of ~4 cm^{-1}. The solution that best fits to the given R^{measured} survives in the next generations and produces "offspring," which are variations of their respective parents (Sheta & De Jong, 1996). Detailed step-by-step procedures of the GA-driven LSQ method used here are shown in Figure 1 and explained in detail below.

3.3.1. Parameters of the GA Routine

There are two main factors that control the solutions of our optimization problem:

1. The optimal number of harmonic oscillators (j) that are required to best fit the data, and
2. the actual values of the oscillator parameters for each j that determines the optical constants of the solution for all ν.

To find the most suitable number of oscillators (j) for each spectrum, the measured spectrum (R^{measured}) is segmented into six spectral ranges (R1–R6) spanning the whole relevant spectral range (Table A1, Appendix A). Boundaries of these spectral ranges are carefully chosen under the guidance of the second derivative of R^{measured} (Figure A1, Appendix A) for each sample studied. The second derivative approach to find the boundaries of spectral ranges is described using an example in Appendix A. For each spectral range, the maximum number of oscillators allowed per spectral range (Table A1, Appendix A) and the minimum χ^2 value of 0.3 (Equation 3) for each spectral range is pre-defined for each spectrum. Therefore, the final total optimum number of oscillator frequencies within these spectral ranges is controlled by the minimum χ^2 fit (Equation 4) achieved for each spectral range of the modeled reflectance (R^{modeled}) for each chromosome (set of oscillator parameters for all j) by the GA-LSQ routine. Setting of ranges, the maximum number of oscillators per range, and χ^2 cutoffs ensured that the program finds the best and simplest possible solution. This procedure was extensively optimized for glasses before being implemented. To allow the oscillators to fall on the boundaries if present, the frequency gene parameter is allowed to search the space oscillators for ±10 cm^{-1} beyond the spectral region specified for each spectral range. This allows the overlap region of ±10 cm^{-1} for each spectral range. Previous studies such as (Ivanovski et al., 2008) have also split the frequency space into multiple regions for fitting the reflectance spectra in case

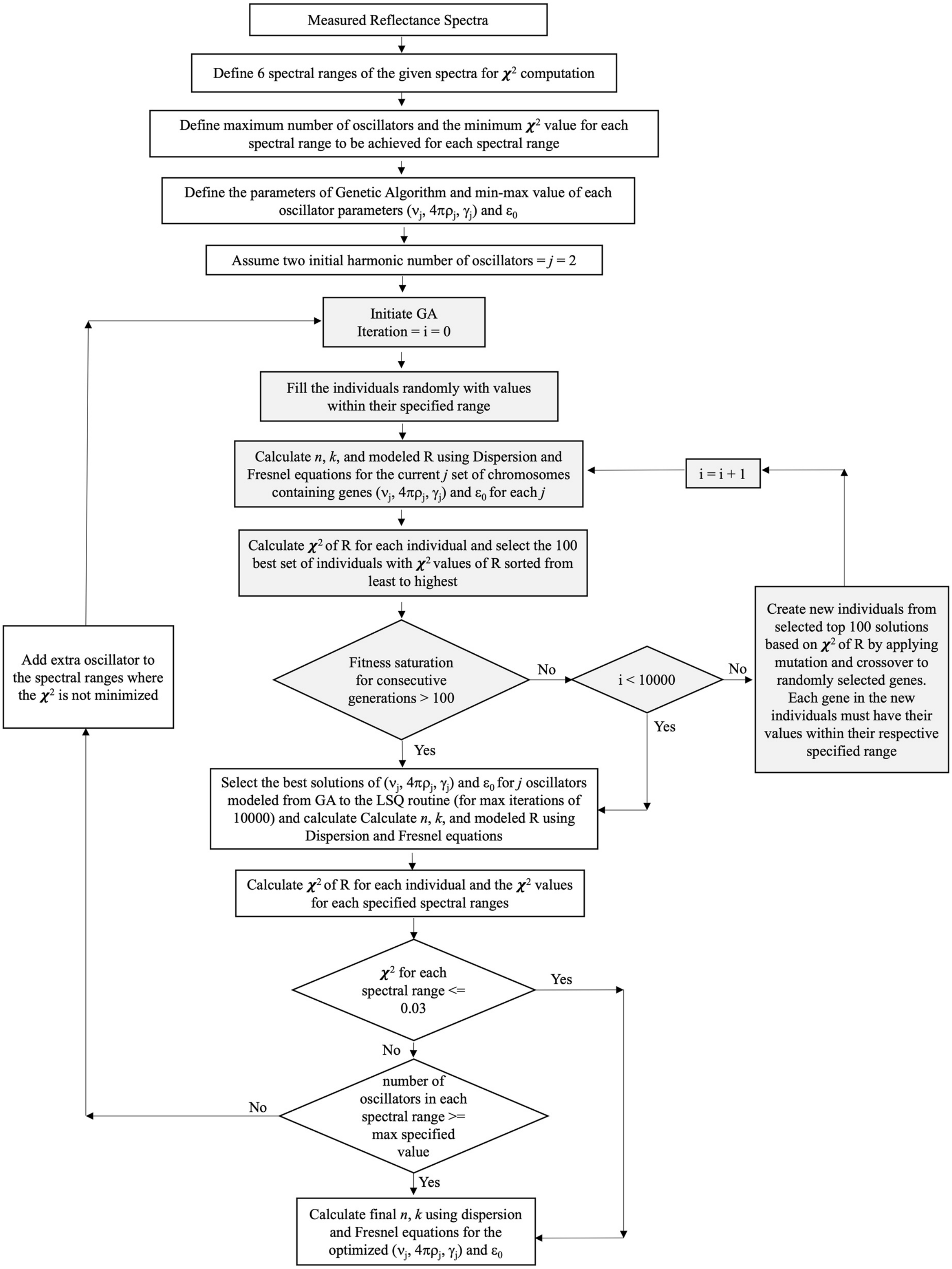

Figure 1. The flow-chart of the implemented genetic algorithm procedure to aid numerical modeling of optical constants.

of monoclinic minerals. We found that solving for a wider spectral range, GA takes longer to converge to find the optimal number of oscillators. The selection of many narrower spectral regions, on the other hand, leads to increased overlapping oscillators for GA to pick. For glasses with broader spectral features, this approach of using the second derivative to guide the manual selection of the spectral range was found to be optimal.

For faster convergence of the GA algorithm, the gene space parameter is initialized, which includes the minimum and maximum limits of the oscillator parameters for each j, as ν_j (extremum wavenumber values for the corresponding spectral range), $4\pi\rho_j$ (min:0, max:2), γ_j (min:0, max:2), and ε_0 (min:1, max:4). We further define additional GA parameters including the total number of generations (=10,000), the number of individuals (solutions) per generation (=100), and the number of parents mating to create new individuals for each generation (=10). The mating of the parents to create new individuals (total of 100) for each subsequent generation is achieved by the process of selection, crossover, and mutation, where the selection operator helps to find the best parents from the pool and the crossover and mutation operators are used to add variations to these parents to create the offspring for the next generation. The details of the selection, crossover, and mutation operators used in this study are explained below.

1. The selection operation determines which individuals are chosen to mate in the new population based on the user-defined criteria. Our algorithm uses the deterministic strategy known as population decimation as used in Güngör and Saka (2004) where the individuals are ranked from the highest to the lowest according to their fitness function value (Equation 5) and the 10 best individuals are kept and used to generate the new individuals through crossover and mutation operations. The rest of the individuals are removed. This population decimation approach allows the GA to converge to the solution faster as only the best individuals from the recent generation are selected to produce offsprings for the next generation.
2. Crossover is one of the most significant steps in GA as it is responsible for producing offspring by recombining parents' genetic material. It is analogous to reproduction and biological crossover. The primary objective of the crossover operation is to enable GAs to effectively explore the search space and produce better individuals in the subsequent generation (Koohestani, 2020). The crossover operator defines how the selected individuals are used to generate the new individuals for the next generation. Our algorithm uses a crossover operation called "two points" as used in Djurišić et al. (1997b), where the two crossover points are picked randomly from the parent chromosomes and the genetic material is exchanged/swapped at these points. The crossover probability is set to 0.15, which determines the probability of selecting a parent for applying the crossover operation. A randomly selected crossover value between 0 and 1 is generated for each selected parent. If this random value is less than or equal to the set crossover probability value (=0.15), then the respective parents are selected.
3. The mutation operator is used to maintain genetic diversity of the chromosomes from one generation to the next. It is analogous to biological mutation. The mutation operator is important because it helps to avoid local minima by preventing the population of chromosomes from becoming too similar to each other, thus slowing or even stopping convergence to the global optimum. Our algorithm uses a mutation method called "adaptive mutation" (Marsili Libelli & Alba, 2000), which calculates the fitness values (f) and collective average fitness value (f_{avg}) for each chromosome after selection and crossover operations are applied. Then it selects the high or low mutation rate for each chromosome based on whether $f < \mathrm{f}_{\mathrm{avg}}$ or $f > \mathrm{f}_{\mathrm{avg}}$. A parameter called "mutation percent genes" is then defined by two values between 0 and 100; the first value is the mutation rate for the low-quality solutions ($f < \mathrm{f}_{\mathrm{avg}}$) and the second value is the mutation rate for the high-quality solutions ($f > \mathrm{f}_{\mathrm{avg}}$). Doing so, adaptive mutation helps to create high quality sets of offspring for the next generation to reach better convergence over the generations.

The GA optimization routine terminates under one of two conditions; (a) either the total generations/iterations reach up to 10,000 or (b) if the fitness saturates for 100 consecutive generations.

3.4. Implementation of GA-Driven LSQ Routine

For the first generation, the GA assumes there are only two oscillators ($j = 2$) in the entire spectral range (400–1,800 cm^{-1}) and initiates the algorithm. The GA algorithm starts by defining minimum and maximum limits of the parameters (ν_j, $4\pi\rho_j$, γ_j, ε_0) for these two oscillators ($j = 2$). A total of 100 chromosomes, each containing the complete set of genes (ν_j, $4\pi\rho_j$, γ_j, ε_0) for two oscillators are randomly generated. The GA then calculates n, k, and R^{modeled}, using the dispersion and Fresnel equations (Equations 1–3), and further calculates the fitness of each randomly generated chromosome (Equations 4 and 5). The 10 best individuals are chosen using the selection operation defined in Section 3.3.1. The GA then proceeds by iteratively generating a new set of individuals (=100) using the 10 best solutions from the previous generations through the application of crossover and mutation operators as described in Section 3.3.1. These iterations are repeated until the fitness saturates for 100 consecutive generations or until the total number of iterations reaches 10,000 runs.

Next, the GA-optimized oscillator parameters are further allowed to converge using an iterative LSQ routine for 10,000 runs by minimizing the χ^2 (Equation 4) value for the optimizing oscillator parameters. After the LSQ routine, new n, k, and R^{modeled} are calculated using Equations 1–3 (Glotch & Rossman, 2009; Glotch et al., 2007). This new GA-driven LSQ R^{modeled} spectrum is then used to calculate the χ^2 value of the fit for each spectral range R1, R2, R3, R4, R5, and R6. If $\chi^2 > 0.03$ for any particular spectral range, and if the number of modeled oscillator frequencies in this spectral range is less than that of the maximum number of oscillators specified for the range, then a new oscillator with the information on the extremum values of their respective oscillator parameters (ν_j, $4\pi\rho_j$, γ_j, ε_0) is appended to the existing gene space of the chromosome string. The extremum values of the oscillator frequencies (ν_j) of the new gene space of the updated chromosomes now include (a) $\nu_j \pm 20\ \text{cm}^{-1}$ of the optimized frequencies from the last generation for its corresponding j and (b) extremum values (min-max) of the ν_j for the newly added oscillators for the corresponding spectral range, which are the same extremum values of the spectral range itself. The GA + LSQ routine is now repeated for this updated gene space containing the new, additional oscillators. Thus, the entire GA-driven LSQ process is iteratively repeated until either (a) the minimum $\chi^2 \leq 0.03$ is reached for all individual spectral ranges (R1–R6) for the optimized chromosomes/oscillator parameters for all j, or b) the maximum number of oscillators allowed for each spectral range is now saturated. If the minimum χ^2 was not achieved for the given number of maximum oscillators for any specific spectral region, we increased the value of the total number of oscillators to those spectral regions to allow GA to pick for more oscillators to pick to achieve the minimum χ^2. The final model-optimized optical constants n and k are then calculated using the oscillator parameters for all j obtained at the end of the iterative GA-driven LSQ approach. A detailed schematic flowchart of the entire GA-driven LSQ approach is shown in Figure 1.

Through this approach, the entire optimization problem is nearly optimized. The code uses the Python packages PyGAD 2.16.3 and the "curve_fit" module of "optimize" sub-package of Scipy 1.7.1 for the implementation of GA and LSQ routines, respectively. The workflow was written in Python 3.9.7. The results of the optical constants and the list of oscillator parameters for each of the silicate glasses studied are discussed below.

4. Results and Discussion

4.1. Measured Reflectance of Glasses

The micro-FTIR MIR spectra of the glasses measured at normal incidence are shown in Figure 2. Irrespective of the variations in their compositions, the measured spectra of all the silicate glasses studied possess similar spectral shape with broad and smooth spectral features. These broad spectral bands are the results of the broader and variable Si-O bond angles and lengths for all TO_4 units (T = Si, Al), in contrast to the well-defined Si-O bond angles and lengths for all TO_4 units responsible for vibrational fine structure in crystalline silicates (Fu et al., 2017; Speck et al., 2011).

Two diagnostic features occur in the spectra of all the silicate glasses:

1. the Christiansen feature (CF) near 8 μm (1,250 cm^{-1}), indicated by black arrows in Figure 2. This feature is an emissivity maximum (or minimum in reflectance) and is an indicator of silicate mineral composition (Conel, 1969). This feature is not affected by variations in grain size, crystal orientation, or crystallinity under terrestrial ambient conditions (Moroz et al., 2009; Salisbury & Wald, 1992).
2. two reststrahlen bands (RBs) formed due to Si-O fundamental stretching and bending vibrations (Salisbury et al., 1991). A broad feature at 8.5–12 μm (~800–1,100 cm^{-1}) results from the asymmetric stretching vibrations of SiO_4 units (King et al., 2004) and is marked as RB1 in Figure 2. This RB band position shifts to lower wavenumbers as a glass becomes depolymerized (e.g., more mafic (Dalby & King, 2006; Fu et al., 2017)). A second RB peak appears near 20–25 μm (400–500 cm^{-1}), resulting from the O-Si-O bending modes (Dalby & King, 2006), and is marked as RB2 in Figure 2.

4.2. Modeled Reflectance and Optical Constants of Glasses

For each glass studied, the measured (micro-FTIR lab spectrum) and modeled spectra, the residual between them, and the modeled optical constants (n and k) are shown in Figures 3–9, respectively. The resulting oscillators modeled to best fit the lab spectrum for all the samples are tabulated in Table 2. The number of oscillators located by the GA-driven LSQ model to adequately fit each glass spectrum include (a) 17 oscillators (χ^2 fitness

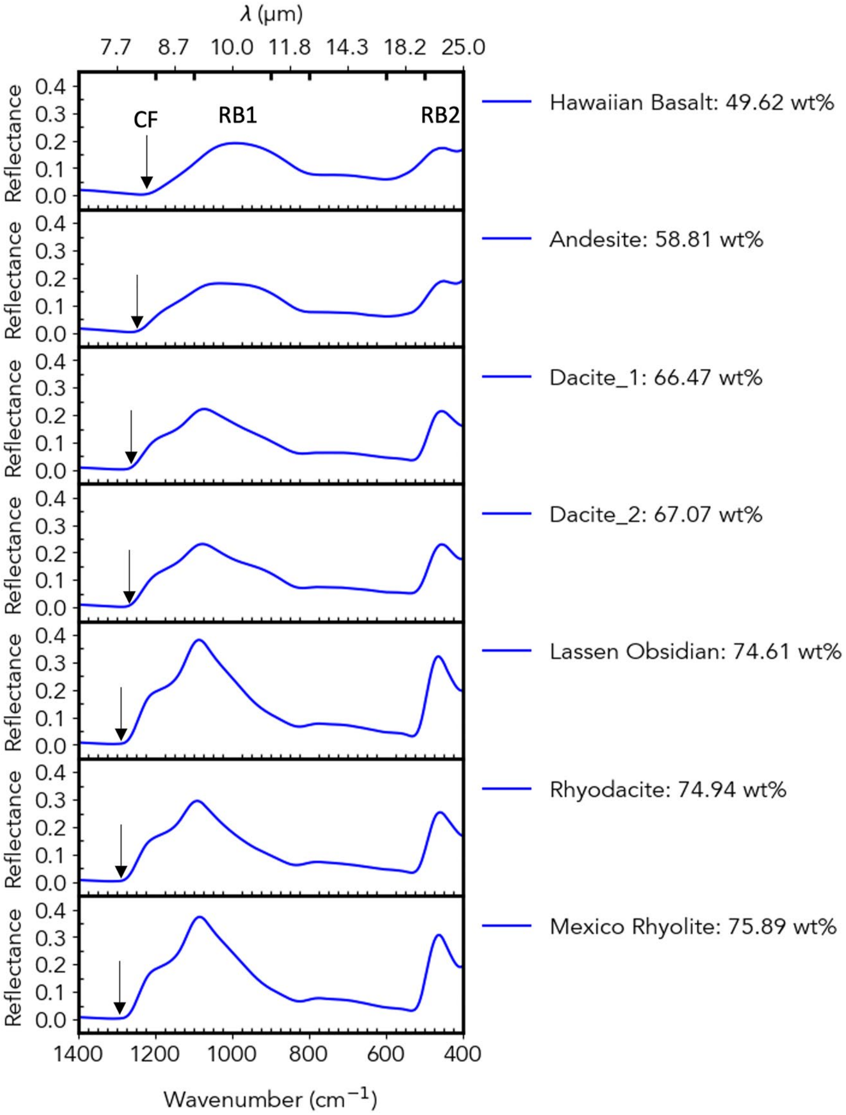

Figure 2. Micro-FTIR mid-infrared spectra of the glasses measured from 400 to 1,800 cm^{-1} (5.56–25 μm) with a spectral sampling of 4 cm^{-1} at normal incidence. The Christiansen feature position is marked as black arrow. The two reststrahlen bands are marked as RB1 and RB2. The wt% value in the legend corresponds to the SiO_2 wt% for each silicate glass studied.

value of 0.149, Figure 3) for Hawaiian basalt, (b) 16 oscillators ($\chi^2 = 0.02$, Figure 4) for andesite, (c) 14 oscillators ($\chi^2 = 0.063$, Figure 5) for dacite_1, (d) 20 oscillators ($\chi^2 = 0.037$, Figure 6) for dacite_2, (e) 15 oscillators ($\chi^2 = 0.209$, Figure 7) for obsidian glass from Lassen, (*f*) 17 oscillators ($\chi^2 = 0.07$, Figure 8) for synthetic rhyodacite, and (g) 17 oscillators ($\chi^2 = 0.173$, Figure 9) for volcanic rhyolitic glass from Mexico. Further, Table 3 tabulates the overall χ^2 (representing the degree of misfit) and also the χ^2 value for each spectral range (Table A1) used in the GA-LSQ routine for all the glass samples studied. Table 3 shows that there is no correlation between the sample composition (SiO_2 wt%) and the degree of misfit for all spectral ranges (R1–R6) studied. (Pollack et al., 1973) modeled the optical constants of basalt glass and obsidian glass, and their results are compared to our modeled results in Figures 3 and 7 respectively. The reflectivity and the derived optical constants of basalt and obsidian in the Pollack et al. (1973) match closely with our modeled results, irrespective of the differences between the methods and the samples used, which provides a qualitative confidence to our GA-LSQ approach. The spectra from Pollack et al. (1973) were retrieved using an online tool https://automeris.io/WebPlotDigitizer/.

Further, the measured spectra and their modeled optical constants (*n* and *k*) are plotted together in three separate plots in Figures 10a–10c, respectively, where the two RBs of the measured spectra are denoted as RB1 and RB2 in Figure 10a and the two peaks for each optical constant *n* and *k* are denoted as Peak 1 and Peak

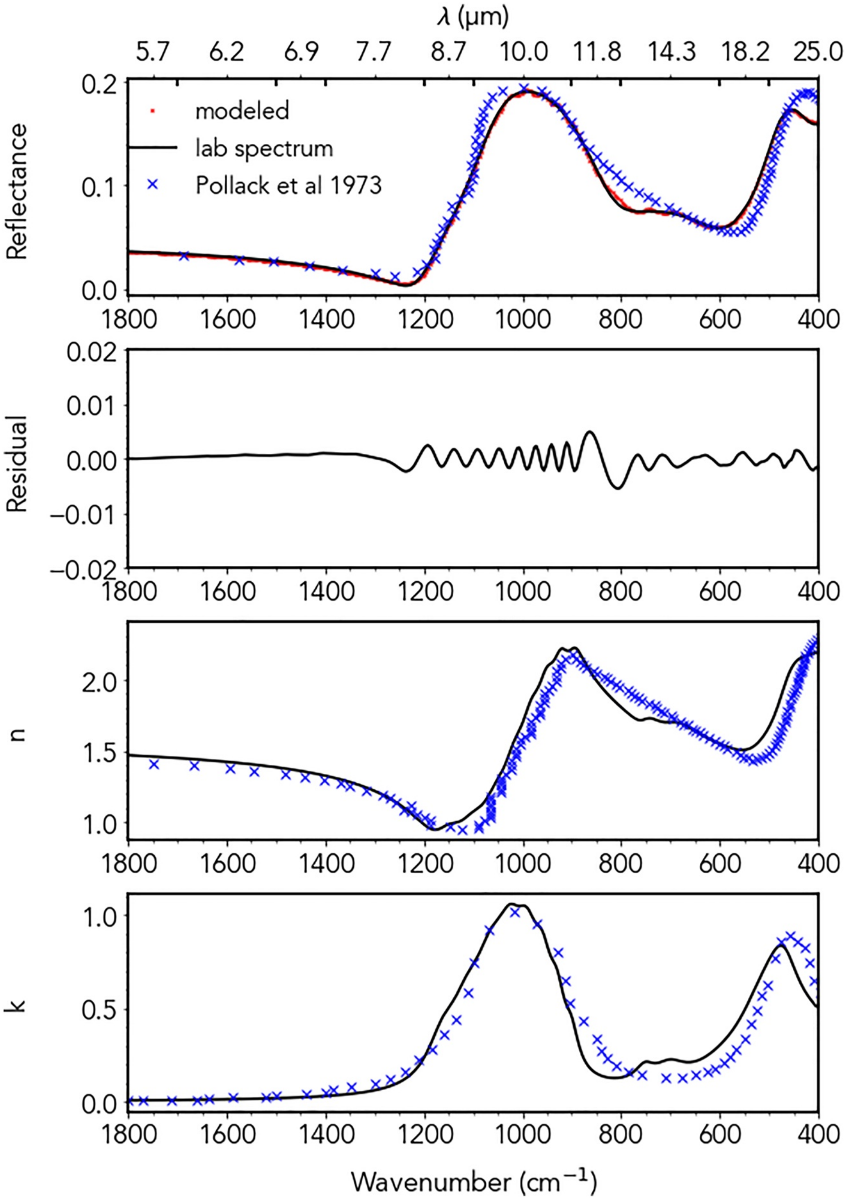

Figure 3. Results of genetic algorithm-driven optical constants modeling for the basaltic glass from Hawaii. (a) MicroFTIR reflectance spectrum (black line) and its modeled spectrum (marked with red cross), the digitized basalt glass reflectivity spectra from Pollack et al. (1973), (b) residuals between the lab spectrum and modeled spectrum from panel (a), (c) modeled optical constant *n* and the digitized optical constant *n* of the basalt glass spectra from Pollack et al. (1973), and (d) modeled optical constant *k* and the digitized optical constant *k* of the basalt glass spectra from Pollack et al. (1973). The spectra from Pollack et al. (1973) were digitized using the online tool https://apps.automeris.io/wpd/.

2 in Figures 10b and 10c, respectively. Among the measured spectra of all glasses (Figure 10a), the andesite and Hawaii basalt show a broader RB1 and RB2 peaks whereas dacite_1, dacite_2, obsidian, rhyodacite, and Mexico rhyolite possess sharp RB1 and RB2 peaks. The vibrational modes of the glasses depend on the nature of the quenching resulting in varying degrees of network connectivity and disorder among these glasses, which further affects the nature of RBs among these glasses (Courtens et al., 2001). This similar spectral trend was also observed for peaks 1 and 2 in the modeled refractive indices (Figures 10b and 10c). The strengths of the first peak show the same trend for reflectance (RB1), *n* (Peak 1) and *k* (Peak 2) following Lassen obsidian (74.61 SiO_2 wt%) > Mexico rhyolite (75.89 SiO_2 wt%) > rhyodacite (74.94 SiO_2 wt%) > dacite_1 (66.47 SiO_2 wt%), dacite_2 (67.07 SiO_2 wt%), and Hawaiian basalt (49.62 SiO_2 wt%) > andesite (58.81 SiO_2 wt%) (Figures 10a–10c). The

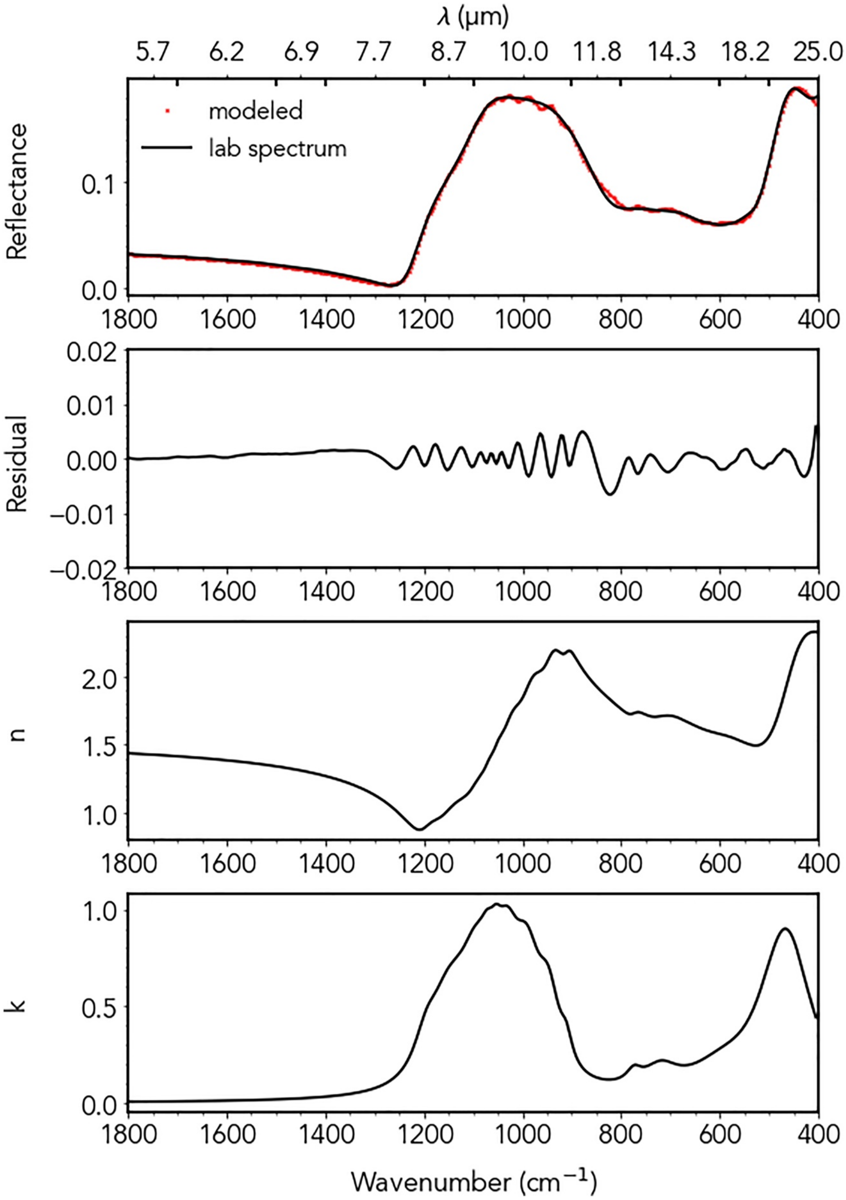

Figure 4. Results of genetic algorithm -driven optical constants modeling for synthetic andesite (a) microFTIR reflectance spectrum (black line) and its modeled spectrum (marked with red cross), (b) residuals between the lab spectrum and modeled spectrum from panel (a), (c) modeled optical constant *n*, and (d) modeled optical constant *k*.

strengths of second peak show the same trend for reflectance (RB2), *n*, and *k* (peak 2) following Lassen obsidian (74.61 SiO_2 wt%) > Mexico rhyolite (75.89 SiO_2 wt%) > rhyodacite (74.94 SiO_2 wt%) > dacite_2 (67.07 SiO_2 wt%) > dacite_1 (66.47 SiO_2 wt%) > andesite (58.81 SiO_2 wt%) > Hawaiian basalt (49.62 SiO_2 wt%) (Figures 10a–10c). The wavenumber dependencies of CF, RBs, and Peak 1 and Peak 2 of *n* and *k* as a function of SiO_2 are further discussed in Section 4.3.

4.2.1. Challenges Due To Amorphous Nature of Glasses

The amorphous band structures of the silicate glasses studied results in the broad spectral feature between 500 and 1,000 cm^{-1}, due to the broader distribution of Si-O bond angles and lengths for all TO_4 (T = Si, Al) units in the glasses (Fu et al., 2017; Speck et al., 2011). The vibrational modes in silicate glasses are influenced by anharmonic effects, disorder, the coordination of the metal cations, and the degree of network connectivity (Courtens et al., 2001). This leads to a broad distribution of frequencies rather than well-defined peaks. This model discrepancy

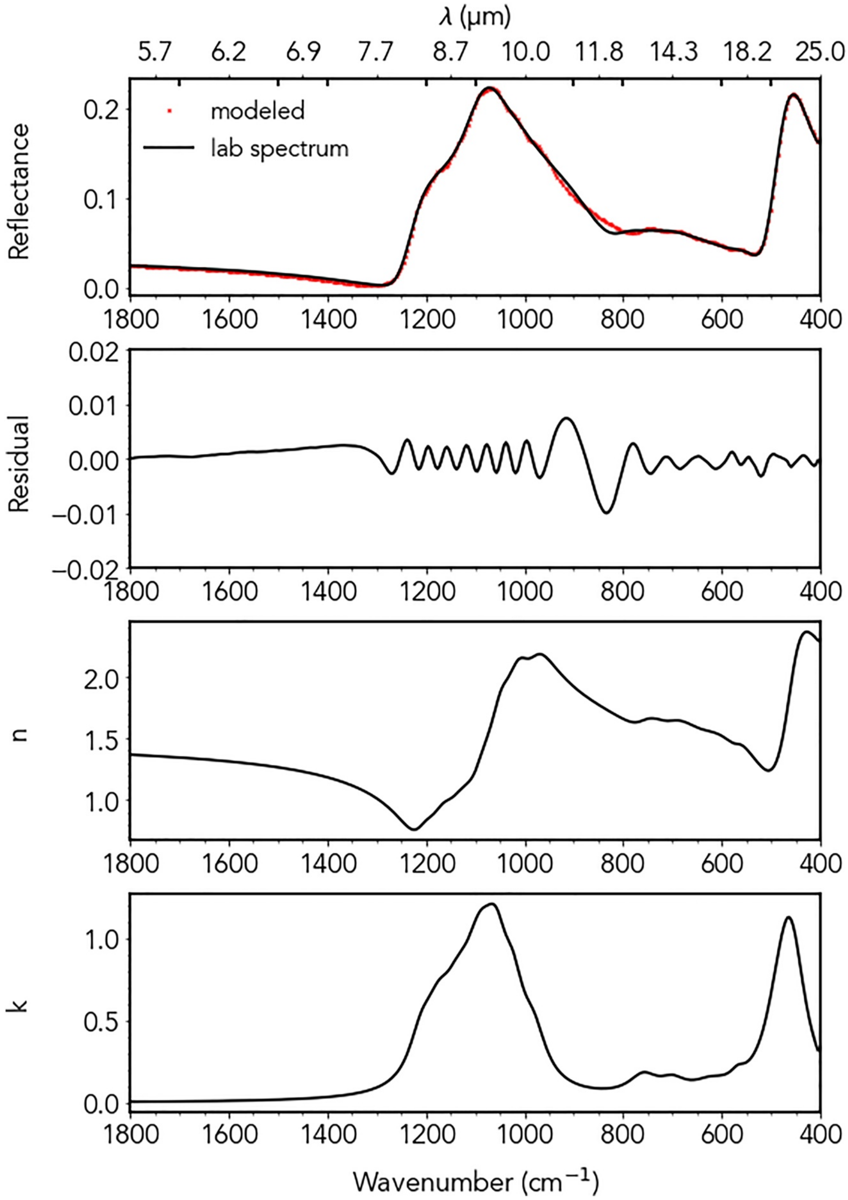

Figure 5. Results of genetic algorithm-driven optical constants modeling for dacite sample dacite_1 in Table 1 (a) microFTIR reflectance spectrum (black line) and its modeled spectrum (marked with red cross), (b) residuals between the lab spectrum and modeled spectrum from panel (a), (c) modeled optical constant *n*, and (d) modeled optical constant *k*.

can be seen in the residual plot (b) in Figures 3–9, where the model discrepancy is most prominent between 800 and 1,000 cm^{-1} for all the glasses. This spectral region corresponds to the spectral range R3 (Table A1 in Appendix A) and Table 3 shows that there no correlation between the degree of misfit (χ^2) and the sample composition for any spectral ranges studied including R3. Adequate χ^2 in this region was most difficult to obtain for the synthetic andesite. The modeled spectra in this region show a sinusoidal shape for the broad RB1 feature (Figures 4 and 10a), whereas the laboratory spectrum is a continuous curve (Figure 4). This type of misfit is not unusual for highly amorphous materials (Glotch et al., 2007) where the oscillators energies may form more of a continuum rather than taking on distinct values. Here, nine unique oscillators were chosen by the model to fit this broad RB1 spectral feature in order to achieve the χ^2 of 0.005. This spectral region was particularly difficult for the model to fit using the classical dispersion theory, which treats the vibrational modes as harmonic oscillators. However, the structural disorder among glasses can lead to non-harmonic motions (Courtens et al., 2001). To overcome this challenge in the GA routine, we allocate the maximum possible number of oscillators to fit these broad regions. However, not all

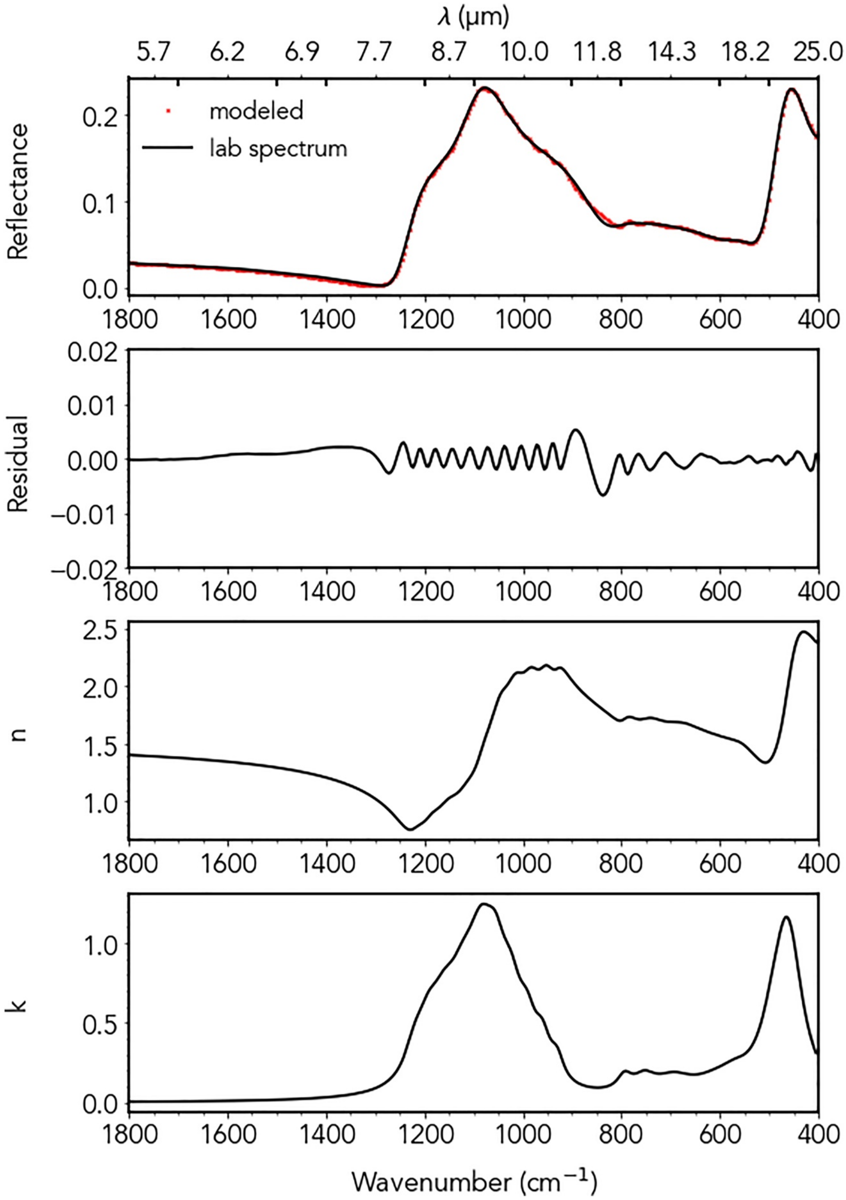

Figure 6. Results of genetic algorithm-driven optical constants modeling for dacite sample dacite_2 in Table 1 (a) microFTIR reflectance spectrum (black line) and its modeled spectrum (marked with red cross), (b) residuals between the lab spectrum and modeled spectrum from panel (a), (c) modeled optical constant *n*, and (d) modeled optical constant *k*.

oscillators are utilized if the required χ^2 value is achieved with fewer oscillators. In cases where χ^2 did not converge with the given total number of oscillators, we increased the total number of oscillators in those spectral regions to achieve the best fit possible. This approach was successfully adopted by previous studies to fit broad spectral features of phyllosilicates for example (Glotch et al., 2007) by manually selecting the possible number of oscillators to fit with an LSQ routine, and the residuals showed a similar sinusoidal shape while fitting those spectral features.

4.2.2. Advantages of the GA-LSQ Model

The GA approach developed in this study for automatically locating the oscillator frequencies and its oscillation parameters can be easily translated to calculate the MIR optical constants of additional volcanic or impact glass samples for the spectral region 400–1,800 cm^{-1}. The only manual inputs required in the model are phase angle, end-points (boundaries) of the spectral regions (R1–R6, Section 3.3.1) to be optimized for fitting, the maximum number of oscillators allowed for each spectral region (refer to Section 3.3.1 and Appendix A), and

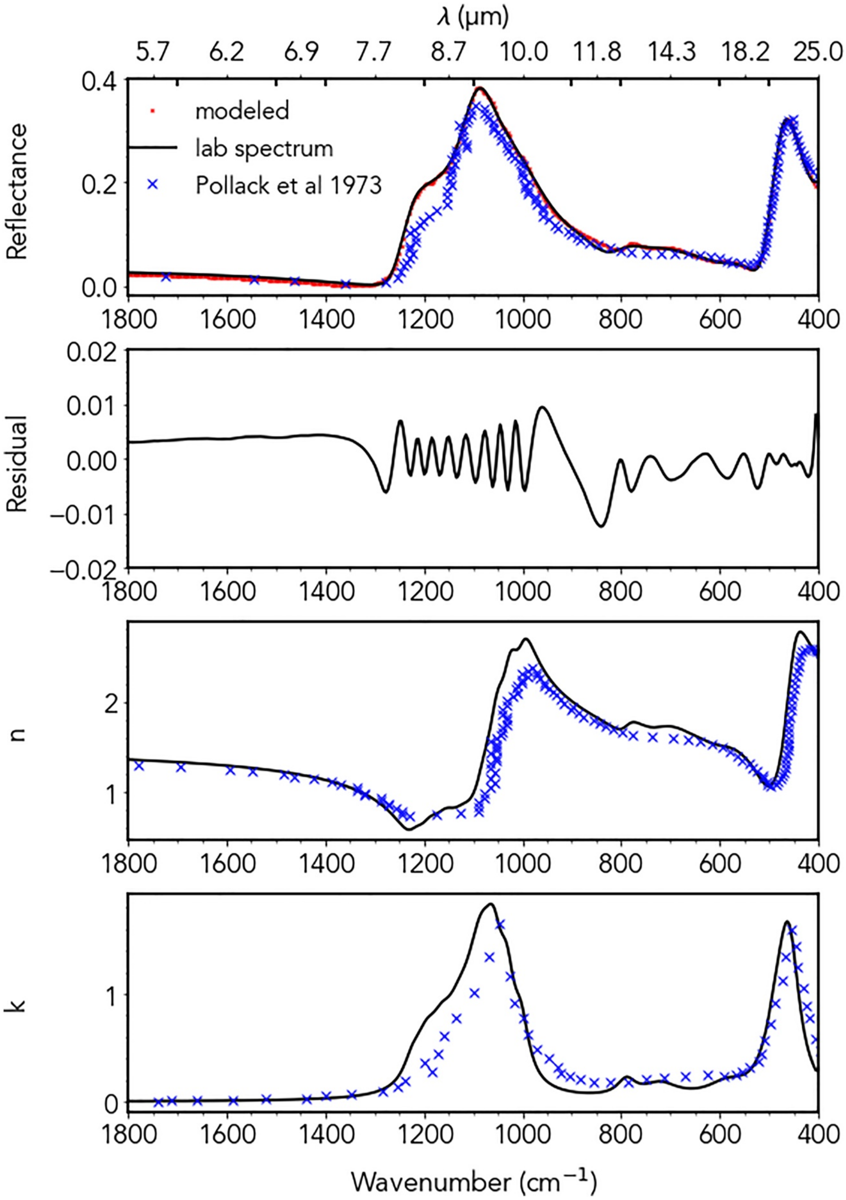

Figure 7. Results of genetic algorithm-driven optical constants modeling for obsidian from Lassen, CA. (a) MicroFTIR reflectance spectrum (black line) and its modeled spectrum (marked with red cross), the digitized obsidian glass reflectivity spectra from Pollack et al. (1973), (b) residuals between the lab spectrum and modeled spectrum from panel (a), (c) modeled optical constant n and the digitized optical constant n of the obsidian glass spectra from Pollack et al. (1973), and (d) modeled optical constant k and the digitized optical constant k of the obsidian glass spectra from Pollack et al. (1973). The spectra from Pollack et al. (1973) were digitized using the online tool https://apps.automeris.io/wpd/.

the minimum χ^2 needed for each spectral region (R1–R6). The end-points of these spectral regions are easily calculated using the second derivative of the measured reflectance spectra (for methodology see Appendix A). Once these parameters are fed to the model, the GA-LSQ routine will automatically start adding the optimal oscillators in each spectral region until it achieves the required χ^2 value or the maximum number of oscillators allowed for that region. Thus, the GA-LSQ routine minimizes human-error while manually choosing the oscillators and their frequencies. Further, the code will work successfully for glass, powder, and isotropic samples with non-normal incidence. In these cases, theta value (incidence and emergence angles) will need to be updated in the appropriate place in the code. The derived MIR optical constants can further be used in the single subtractive

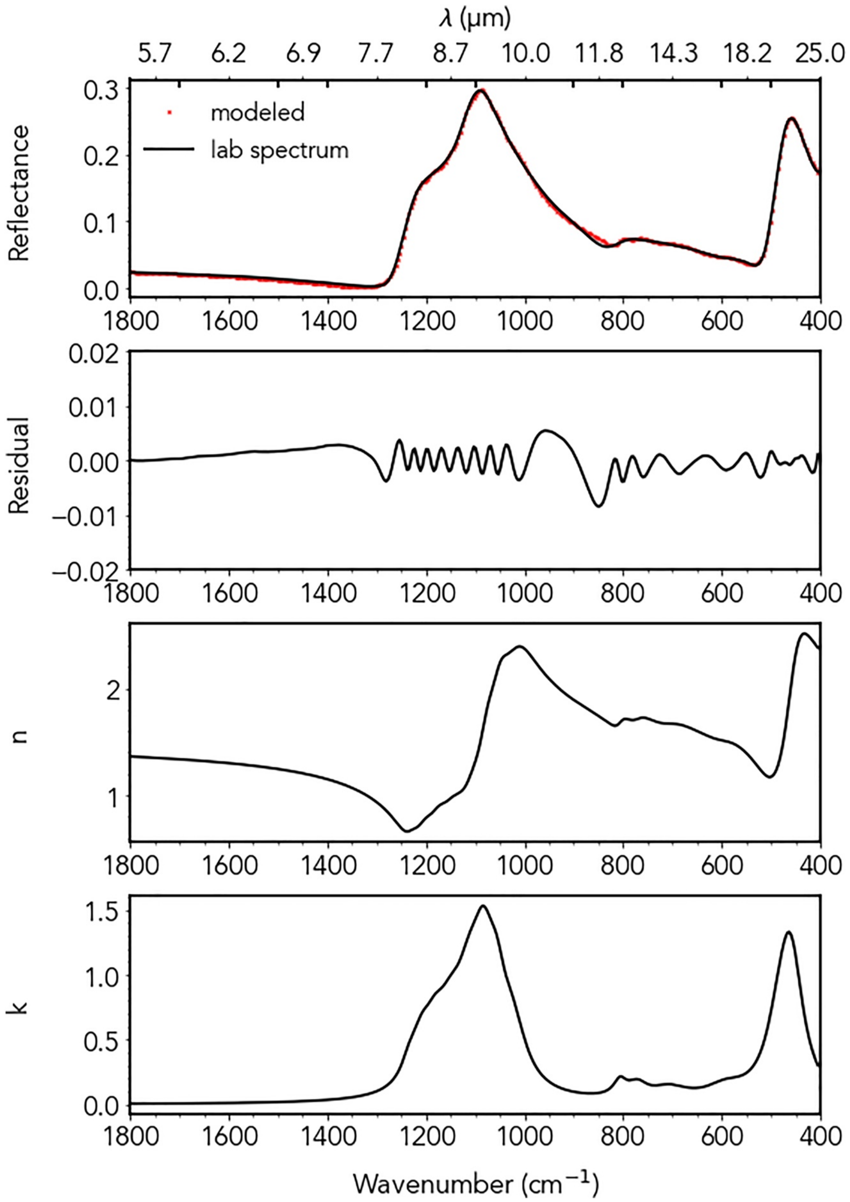

Figure 8. Results of genetic algorithm-driven optical constants modeling for rhyodacite (a) microFTIR reflectance spectrum (black line) and its modeled spectrum (marked with red cross), (b) residuals between the lab spectrum and modeled spectrum from panel (a), (c) modeled optical constant *n*, and (d) modeled optical constant *k*.

Kramer-Kronig (SSKK) transformation with a Hapke model to derive the wavelength-dependent UV-VNIR optical constants of the glasses for varying phase angle observations and particle sizes (Sklute et al., 2015; Ye et al., 2021).

4.3. Wavenumber Dependencies of CF, RBs, and Optical Constants wrt SiO_2 wt%

In this section, the wavenumber dependencies of spectral parameters such as CF, RBs, and Peak 1 and Peak 2 positions of optical constants *n* and *k* is discussed as a function of SiO_2 wt% as shown in Figures 11–13, respectively. The wavenumber positions of these spectral parameters are calculated by fitting the polynomial function for the data points covering the corresponding peaks and finding its maximum value of the function, except for CF, for which minimum of the function is derived. Such traditional approach of finding the CFs and RBs have used in many spectroscopy works, including Donaldson Hanna et al. (2012).

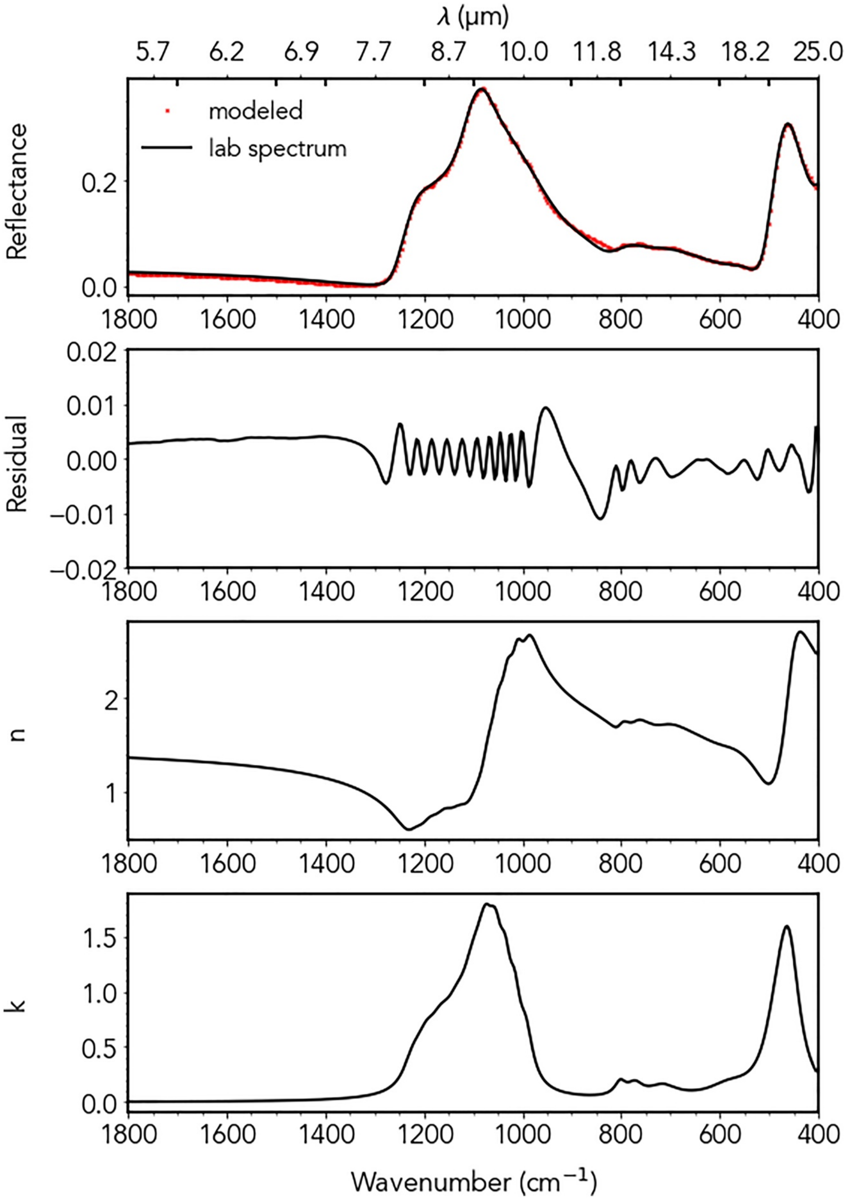

Figure 9. Results of genetic algorithm-driven optical constants modeling for rhyolitic volcanic glass from Mexico. (a) MicroFTIR reflectance spectrum (black line) and its modeled spectrum (marked with red cross), (b) residuals between the lab spectrum and modeled spectrum from panel (a), (c) modeled optical constant *n*, and (d) modeled optical constant *k*.

4.3.1. CF and RBs Versus SiO_2

The CF positions marked on the spectra in Figure 2 are plotted against sample SiO_2 wt% in Figure 11. The wavelength positions of RB1 and RB2 marked in Figure 10a are plotted against their corresponding SiO_2 wt% of the respective glasses and are shown in Figures 12a and 12b, respectively. CF position (basalt < andesite < dacite_1, dacite_2 < obsidian, rhyodacite, and rhyolite) of the glasses studied shifts systematically to higher wavenumbers with increasing SiO_2 wt%, as observed in previous studies (Donaldson Hanna et al., 2012; Greenhagen et al., 2010). Similar to the trend observed in the CF versus SiO_2 plot, the RB1 shift to higher wavenumbers with increasing SiO_2 wt% (Figure 12a) as reported in previous studies (Dalby & King, 2006; Fu et al., 2017). However, RB2 versus SiO_2 wt% plot (Figure 12b) shows that basalt and andesite have similar RB2 position irrespective of their varying SiO_2 wt% and the RB2 shift to higher wavenumbers with increasing SiO_2 wt% in the order basalt, andesite < dacite_1, dacite_2 < obsidian, rhyodacite, and rhyolite. Figure 10a shows that andesite and basalt

Table 2
Derived Oscillator Parameters of Glasses

Dacite_1 ($\varepsilon_0 = 2.412$)					
ν	γ	$4\pi\rho$	ν	γ	$4\pi\rho$
457.498	0.249	0.866	945.212	0.057	0.094
594.150	0.244	0.061	982.137	1.273	0.000
611.474	0.276	0.000	987.699	0.069	0.149
616.806	0.322	0.000	1,027.740	0.057	0.097
622.914	0.236	0.024	1,051.853	0.031	0.020
719.800	0.124	0.049	1,069.466	0.031	0.015
773.433	0.047	0.011	1,092.224	0.066	0.076
805.738	2.416	0.000	1,130.371	0.062	0.021
836.398	2.425	0.000	1,151.492	0.065	0.031
841.756	2.533	0.000	1,138.970	2.740	0.000
861.995	2.389	0.000	1,190.313	0.051	0.016
910.210	0.032	0.018	1,233.634	2.778	0.000
Andesite ($\varepsilon_0 = 2.197$)			Lassen ($\varepsilon_0 = 2.246$)		
ν	γ	$4\pi\rho$	ν	γ	$4\pi\rho$
455.601	0.152	0.663	454.770	0.106	0.786
566.865	0.065	0.011	500.875	0.551	0.000
624.365	0.139	0.029	587.984	0.158	0.056
699.477	0.096	0.025	720.908	0.121	0.054
759.085	0.095	0.036	788.312	0.057	0.030
980.191	0.065	0.081	819.615	3.441	0.000
986.197	1.491	0.000	1,001.376	0.039	0.105
999.190	0.251	0.000	978.629	3.735	0.000
1,020.539	0.054	0.100	1,029.593	0.036	0.145
1,054.077	0.054	0.126	1,055.160	0.038	0.154
1,085.975	0.061	0.091	1,078.961	0.047	0.110
1,130.760	0.063	0.047	1,123.279	0.055	0.037
1,170.045	0.053	0.030	1,159.561	0.047	0.028
1,204.306	0.046	0.014	1,190.253	0.038	0.015
			1,217.337	0.033	0.006
Rhyodacite ($\varepsilon_0 = 2.222$)			Dacite_2 ($\varepsilon_0 = 2.328$)		
ν	γ	$4\pi\rho$	ν	γ	$4\pi\rho$
455.578	0.129	0.696	456.375	0.146	0.673
515.242	0.331	0.000	493.141	0.089	0.009
593.415	0.162	0.046	503.943	0.239	0.022
706.978	0.131	0.039	607.296	0.197	0.050
770.844	0.064	0.022	569.180	0.115	0.020
805.667	0.040	0.016	694.596	0.136	0.046
830.503	4.000	0.000	752.876	0.075	0.025
854.298	3.878	0.000	793.170	0.045	0.014
884.107	3.962	0.000	827.975	3.746	0.000
1,022.769	0.066	0.154	877.232	3.741	0.000

Table 2
Continued

Dacite_1 ($\varepsilon_0 = 2.412$)					
ν	γ	$4\pi\rho$	ν	γ	$4\pi\rho$
1,054.316	0.043	0.111	929.873	0.035	0.022
1,078.749	0.044	0.124	959.384	0.041	0.041
1,107.398	0.051	0.056	990.104	0.046	0.060
1,145.751	0.051	0.037	1,021.695	0.049	0.087
1,177.192	0.043	0.024	1,052.015	0.051	0.114
1,204.505	0.036	0.013	1,080.791	0.056	0.100
1,229.287	0.029	0.004	1,117.709	0.059	0.050
	Rhyolite—Mexico ($\varepsilon_0 = 2.240$)		1,155.268	0.053	0.035
ν	γ	$4\pi\rho$	1,187.427	0.045	0.019
455.537	0.109	0.753	1,216.105	0.037	0.008
519.995	0.271	0.001		Basalt—Hawaii ($\varepsilon_0 = 2.495$)	
583.785	0.176	0.054	ν	γ	$4\pi\rho$
715.376	0.104	0.039	424.086	0.564	0.908
771.536	0.051	0.020	467.972	0.162	0.224
801.418	0.034	0.014	508.820	0.246	0.168
869.635	3.606	0.000	598.005	0.227	0.024
991.984	0.034	0.080	701.249	0.111	0.034
1,014.432	0.027	0.083	751.829	0.062	0.016
1,033.564	0.027	0.096	774.839	3.870	0.000
1,052.309	0.029	0.100	900.025	0.040	0.032
1,071.318	0.034	0.093	928.700	0.044	0.062
1,095.067	0.043	0.049	957.241	0.049	0.085
1,129.760	0.048	0.033	987.679	0.056	0.100
1,161.346	0.044	0.026	1,021.015	0.064	0.097
1,190.787	0.039	0.016	1,058.999	0.072	0.073
1,218.243	0.035	0.007	1,107.033	0.076	0.045
			1,157.832	0.066	0.023
			1,152.971	3.778	0.000

Table 3
Degree of Misfit Between Measured and the Modeled Spectra for All Spectral Ranges

		χ^2						
Sample	SiO_2 wt%	Overall	R1	R2	R3	R4	R5	R6
Basalt	49.62	0.020	0.000	0.001	0.004	0.000	0.002	0.013
Andesite	58.81	0.023	0.001	0.002	0.005	0.001	0.005	0.008
Dacite 1	66.47	0.063	0.001	0.005	0.019	0.000	0.002	0.035
Dacite 2	67.07	0.037	0.000	0.003	0.004	0.000	0.002	0.027
Lassen Obsidian	74.61	0.209	0.001	0.015	0.022	0.000	0.004	0.165
Rhyodacite	74.94	0.070	0.000	0.004	0.012	0.000	0.001	0.052
Mexico Rhyolite	75.89	0.173	0.001	0.011	0.018	0.000	0.003	0.139

Note. The spectral ranges of R1, R2, R3, R4, R5, and R6 for each glass studied are given in Table A1 in Appendix A.

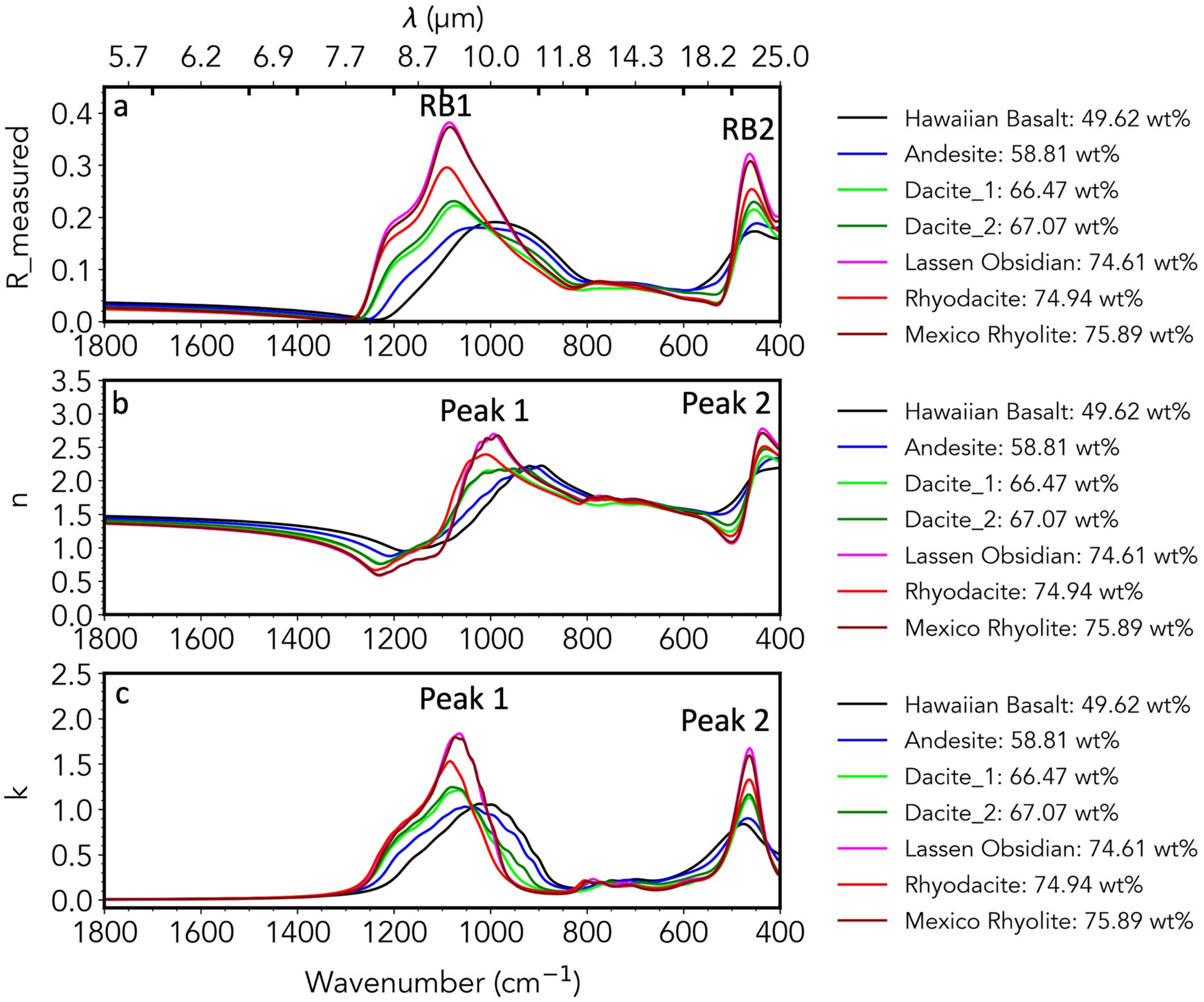

Figure 10. (a) Measured micro-FTIR spectra of all glasses studied where two reststrahlen band positions are indicated. (b) Modeled optical constant *n* showing two peaks (Peak 1 and Peak 2), (c) Modeled optical constant *k* showing two peaks (Peak 1 and Peak 2). The wt% value in the legend corresponds to the SiO_2 wt% for each silicate glass studied.

share a similar spectral shape unlike other glasses studied. The nature of quenching of these basalts must be influencing the position of RB2 unlike the RB1 position. This suggests that the RB1 position is the better SiO_2

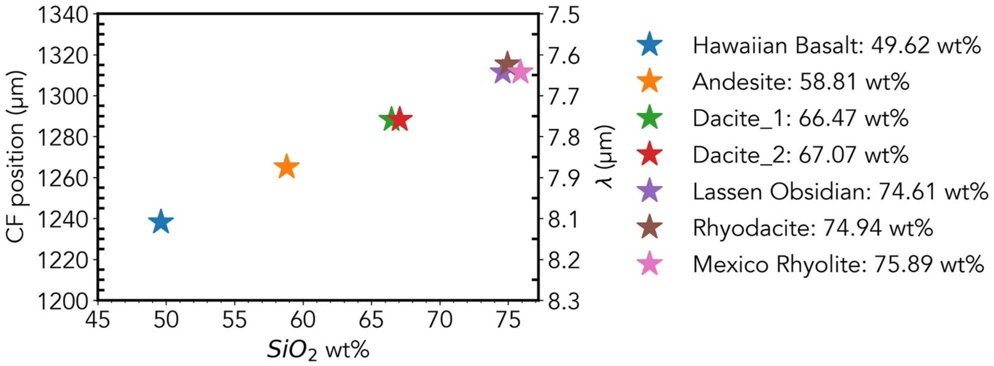

Figure 11. Wavelength/wavenumber positions of Christiansen feature (CF) in the measured MIR reflectance spectra of the silicates studied are plotted against their SiO_2 wt%. CF positions of the measured reflectance spectra are marked by a black arrow in Figure 2.

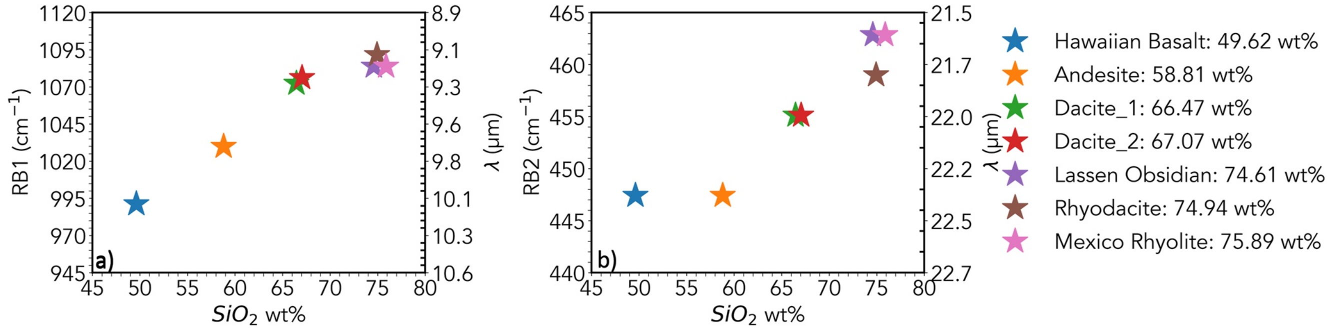

Figure 12. Wavelength/wavenumber positions of RB1 and RB2 in the measured MIR reflectance spectra of the silicates studied are plotted against their SiO_2 wt% in panels (a, b), respectively. RB1 and RB2 positions of the measured reflectance spectra are marked by a black arrow in Figure 10a.

wt% indicator. The nature of the RB2 position as a function of SiO_2 wt% is poorly understood. Among the two dacites studied, the dacite_2 sample possesses a slightly higher RB1 wavenumber position compared to dacite_1; however, the RB2 positions of dacite_1 and dacite_2 are similar. Among the obsidian, rhyodacite, and rhyolite glass studied with SiO_2 wt.% in the range of 74.61–75.89 wt%, obsidian and rhyolite share similar RB1 and RB2 wavenumber positions. On the other hand, rhyodacite has a higher RB1 wavenumber position and a lower RB2 wavenumber position compared to rhyodacite and rhyolite glass spectra.

4.3.2. Optical Constants Versus SiO_2

The wavenumber positions of Peak 1 and Peak 2 of optical constant *n* (denoted on Figure 10b) are plotted against the SiO_2 wt% of their respective glasses in Figures 13a and 13b, respectively. Similarly, the wavenumber positions of Peak 1 and Peak 2 of optical constant *k* (denoted on Figure 10c) are plotted against the SiO_2 wt% of their respective glasses in Figures 13c and 13d, respectively. Figures 13a and 13b shows that Peaks 1 and 2 of optical constant *n* shifts to higher wavenumbers with increase in SiO_2 wt% of the glasses. On the other hand, Figures 13c and 13d shows that wavenumber position of Peak 1 of the optical constant *k* broadly increases with SiO_2 wt%, however, wavenumber position of Peak 2 of *k* broadly decreases with increasing SiO_2 wt%. Figures 13c

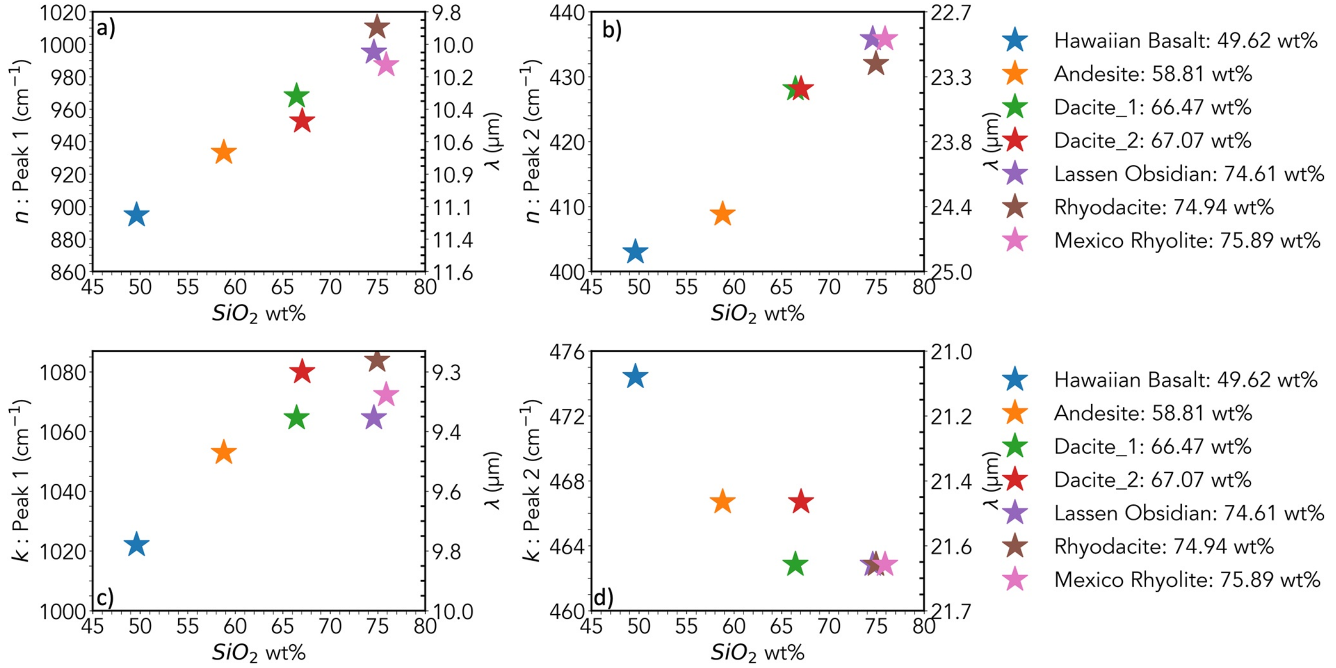

Figure 13. (a, b) Wavelength/wavenumber positions of peak 1 and peak 2 of the modeled optical constant *n* (indicated in Figure 10b) are plotted against their SiO_2 wt%, respectively. (c, d) Wavelength/wavenumber positions of peak 1 and peak 2 of the modeled optical constant *k* (indicated in Figure 10c) are plotted against their SiO_2 wt%, respectively.

and 13d further highlights that dacite_1 and dacite_2, irrespective of having similar SiO_2 wt% shows considerably different Peak 1 and Peak 2 values of *k*. This behavior of dacite_1 and dacite_2 can be explained by their slightly different spectral shape in their measured reflectance spectra shown in Figure 10a. These dacite glasses further highlight that glasses can have considerably different spectral shapes irrespective of their similar sample compositions, depending on their degree of network connectivity and disorder (Nocuń & Handke, 2001; Stoch & Środa, 1999). Furthermore, Figures 13c and 13d shows obsidian, rhyodacite, and rhyolite, which have similar SiO_2 wt.%, have similar Peak 2 values but varying Peak 1 values in the order of rhyodacite > rhyolite > obsidian. The refractive index *n* and extinction coefficient *k* are both important parameters that describe how light interacts with a material. The refractive index *n* describes how much light is refracted, while the extinction coefficient *k* describes how much light is absorbed by the material.

5. Implications and Future Work

The lack of accessible *n* and *k* data for various relevant glasses has impeded the utilization of radiative transfer modeling techniques to determine quantitative abundances from particulate surfaces in the MIR spectral region. This paper introduces optical constants of commonly found silicate glasses on different planetary targets including the Earth, Moon, Mars, and Mercury that enable the application of such modeling techniques to estimate abundances of silicate glasses in the mixed spectra (e.g., Glotch et al., 2016). These estimated abundances can be employed on the planetary surfaces to constrain volcanic/impact processes. The comprehensive explanation of the technique utilized in this paper, accompanied by the availability of our GA-LSQ code (Varatharajan et al., 2023a), holds immense potential for expanding the existing optical constants library of silicate glasses in the near future. Further, in our future work, the derived MIR optical constant *k* will be used in the SSKK transformation of Hapke model to derive the wavelength-dependent UV-VNIR optical constants of these silicate glasses for varying phase angle observations and particle sizes as explained in Sklute et al. (2015) and Ye et al. (2021).

6. Conclusions

We have derived the wavelength dependent MIR (400–1,800 cm^{-1}) optical constants of seven glasses with increasing SiO_2 wt%; a natural Hawaiian basalt < synthetic andesite < two synthetic dacites < a natural obsidian < a synthetic rhyodacite < a natural Mexican rhyolite. The optical constants were derived using dispersion theory and a Fresnel reflectance model for high-symmetry materials (isotropic) at normal incidence. We further adopted a GA approach to automatically find the natural oscillators and their parameters (frequency, damping coefficient, strength) and high-frequency dielectric constant for each measured spectrum, which were then further optimized using a non-linear least squares routine. This improved approach of combining GA with LSQ minimizes the human error in manually finding the possible oscillators and their parameters for the LSQ to approach. The derived MIR optical constants can be used in light scattering models to quantify the mineral abundances of the volcanic surfaces from the orbit. The successful application of the GA-LSQ model can be adapted and applied to retrieve the optical constants of other high-symmetry (isotropic) materials based upon the protocols laid out in this paper.

Appendix A: Method for Selection of Spectral Ranges for Aiding Genetic Algorithm

Manual selection of spectral ranges R1, R2, R3, R4, R5, and R6 for aiding the selection of the optimum number oscillator frequencies in each spectral range by genetic algorithm (GA) are marked in Figure A1. The defined spectral ranges for R1–R6 for each glass spectra and the number of maximum oscillators (N_osc) are detailed in Table A1.

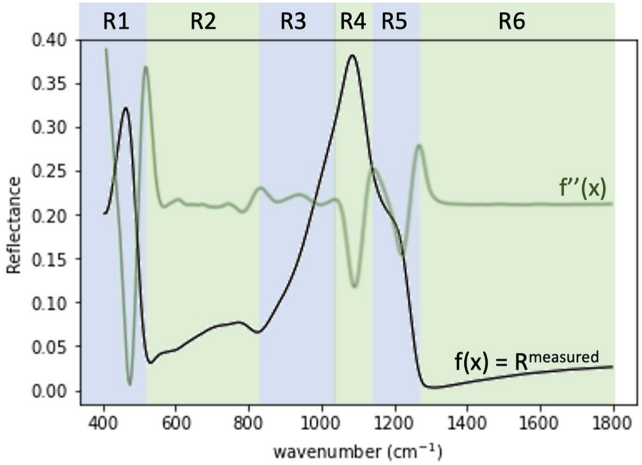

Figure A1. An example of a laboratory spectrum ($f(x) = R^{\text{measured}}$) for which the ranges are shown. The black spectrum is the measured laboratory spectrum. The green spectrum ($f''(x)$) is the second derivative of the measured laboratory spectrum (black line). The combination of the lab spectrum and its corresponding second derivative are used to guide the careful selection of these ranges for each laboratory spectrum to be modeled for optical constants. The end points of each range correspond to the consecutive local maxima points in their respective second derivative spectra as shown in the Figure. This second derivative approach allows us to segment the spectral regions to multiple parts were oscillators are expected to be present, and therefore guides in minimizing the χ^2 fitness value for each spectral range (See Section 3.3.1 in the main manuscript). However, in the genetic algorithm algorithm routine, the end points of these ranges are given with the flexibility of up to 20 cm^{-1} wavenumbers. Therefore, the selection of the oscillator frequencies is affected by the extreme points of these ranges. The ranges selected for each glass spectrum and the defined maximum number of oscillators allowed for each range are tabulated in Table A1.

Table A1

Spectral Ranges (R1, R2, R3, R4, R5, and R6) and the Maximum Number of Oscillators Defined for Each Range for All Glasses Studied Are Tabulated

Range		Dacite_1	Dacite_2	Rhyodacite	Basalt from Hawaii	Obsidian from Lassen	Rhyolite from Mexico	Andesite burnt lava
R1	Range cm^{-1}	400–528	400–516	400–516	400–532	400–516	400–516	400–605
	N_osc	1	1	1	2	1	1	1
R2	Range cm^{-1}	528–817	516–833	516–833	532–782	516–833	516–833	605–806
	N_osc	5	6	5	6	5	5	5
R3	Range cm^{-1}	817–1,029	833–1,002	833–1,033	782–921	833–1,045	833–1,045	806–902
	N_osc	4	6	5	5	4	4	5
R4	Range cm^{-1}	1,029–1,103	1,002–1,145	1,033–1,145	921–1,068	1,045–1,103	1,045–1,103	902–1,103
	N_osc	1	2	2	4	2	2	7
R5	Range cm^{-1}	1,103–1,261	1,145–1,265	1,145–1,265	1,068–1,214	1,103–1,265	1,103–1,265	1,103–1,261
	N_osc	4	6	4	5	5	5	5
R6	Range cm^{-1}	1,261–1,800	1,265–1,800	1,265–1,800	1,214–1,800	1,265–1,800	1,265–1,800	1,261–1,800
	N_osc	0	0	0	0	0	0	0

Data Availability Statement

The measured reflectance spectra for the whole spectral region of 400–4,000 cm^{-1} and their optical constants n and k for the wavenumber region 400–1,800 cm^{-1} for all glasses studied are available at Varatharajan et al. (2023b). The Jupyter notebook containing the code and the instructions to adapt the code for new samples are available at Varatharajan et al. (2023a).

Acknowledgments

This work was supported by NASA PDART Grant 80NSSC21K0877 to E. C. Sklute and the RISE2 SSERVI cooperative agreement 80NSSC19M0215. The authors sincerely thank Melissa Lane and Anonymous reviewer for their careful attention and inputs that helped shape the manuscript.

References

Arnold, J. A. (2014). Refining mid-infrared emission spectroscopy as a tool for understanding planetary surface mineralogy through laboratory studies, computational models, and lunar remote sensing data. (Publication Number 3632507) [Ph.D., State University of New York at Stony Brook]. Dissertations & Theses @ SUNY Stony Brook; ProQuest Dissertations & Theses Global. Retrieved from http://proxy.library.stonybrook.edu/login?url=https://www.proquest.com/dissertations-theses/refining-mid-infrared-emission-spectroscopy-as/docview/1594942043/se-2?accountid=14172%20https://search.library.stonybrook.edu/openurl/01SUNY_STB/01SUNY_STB:01SUNY_STB??genre=dissertations&atitle=&author=Arnold%2C+Jessica+Anne&volume=&issue=&spage=&date=2014&rft.btitle=&rft.jtitle=&issn=&isbn=978-1-321-11910-7&sid=ProQuest+Dissertations+%26+Theses+Global

Arnold, J. A., Glotch, T. D., & Plonka, A. M. (2014). Mid-infrared optical constants of clinopyroxene and orthoclase derived from oriented single-crystal reflectance spectra. *American Mineralogist*, *99*(10), 1942–1955. https://doi.org/10.2138/am-2014-4828

Aronson, J., & Strong, P. (1975). Optical constants of minerals and rocks. *Applied Optics*, *14*(12), 2914–2920. https://doi.org/10.1364/ao.14.002914

Besse, S., Doressoundiram, A., & Benkhoff, J. (2015). Spectroscopic properties of explosive volcanism within the Caloris basin with MESSENGER observations. *Journal of Geophysical Research: Planets*, *120*(12), 2102–2117. https://doi.org/10.1002/2015je004819

Bhattacharya, S., Saran, S., Dagar, A., Chauhan, P., Chauhan, M., Ajai, A., & Kumar, S. K. (2013). Endogenic water on the Moon associated with non-mare silicic volcanism: Implications for hydrated lunar interior. *Current Science*, *105*, 685–691.

Brož, P., Bernhardt, H., Conway, S. J., & Parekh, R. (2021). An overview of explosive volcanism on Mars. *Journal of Volcanology and Geothermal Research*, *409*, 107125. https://doi.org/10.1016/j.jvolgeores.2020.107125

Byrnes, J. M., Ramsey, M. S., King, P. L., & Lee, R. J. (2007). Thermal infrared reflectance and emission spectroscopy of quartzofeldspathic glasses. *Geophysical Research Letters*, *34*(1). L01306. https://doi.org/10.1029/2006GL027893

Cannon, K. M., Mustard, J. F., Parman, S. W., Sklute, E. C., Dyar, M. D., & Cooper, R. F. (2017). Spectral properties of Martian and other planetary glasses and their detection in remotely sensed data. *Journal of Geophysical Research: Planets*, *122*(1), 249–268. https://doi.org/10.1002/2016je005219

Chao, E. C. (1967). Shock effects in certain rock-forming minerals: Hypervelocity impacts by meteorites are reflected by the effects of shock and temperature on minerals. *Science*, *156*(3772), 192–202. https://doi.org/10.1126/science.156.3772.192

Christensen, P. R., Bandfield, J. L., Hamilton, V. E., Ruff, S. W., Kieffer, H. H., Titus, T. N., et al. (2001). Mars global surveyor thermal emission spectrometer experiment: Investigation description and surface science results. *Journal of Geophysical Research*, *106*(E10), 23823–23871. https://doi.org/10.1029/2000JE001370

Christensen, P. R., Jakosky, B. M., Kieffer, H. H., Malin, M. C., McSween, H. Y., Nealson, K., et al. (2004a). The thermal emission imaging system (THEMIS) for the Mars 2001 Odyssey Mission. *Space Science Reviews*, *110*(1), 85–130. https://doi.org/10.1023/b:spac.0000021008.16305.94

Christensen, P. R., Mehall, G. L., Silverman, S. H., Anwar, S., Cannon, G., Gorelick, N., et al. (2003). Miniature thermal emission spectrometer for the Mars exploration rovers. *Journal of Geophysical Research*, *108*(E12), 8064. https://doi.org/10.1029/2003je002117

Christensen, P. R., Wyatt, M., Glotch, T., Rogers, A., Anwar, S., Arvidson, R., et al. (2004b). Mineralogy at Meridiani Planum from the mini-TES experiment on the opportunity rover. *Science*, *306*(5702), 1733–1739. https://doi.org/10.1126/science.1104909

Conel, J. E. (1969). Infrared emissivities of silicates: Experimental results and a cloudy atmosphere model of spectral emission from condensed particulate mediums. *Journal of Geophysical Research*, *74*(6), 1614–1634. https://doi.org/10.1029/JB074i006p01614

Courtens, E., Foret, M., Hehlen, B., & Vacher, R. (2001). The vibrational modes of glasses. *Solid State Communications*, *117*(3), 187–200. https://doi.org/10.1016/s0038-1098(00)00434-8

Dalby, K. N., & King, P. L. (2006). A new approach to determine and quantify structural units in silicate glasses using micro-reflectance Fourier-Transform infrared spectroscopy. *American Mineralogist*, *91*(11–12), 1783–1793. https://doi.org/10.2138/am.2006.2075

D'Incecco, P., Filiberto, J., López, I., Eggers, G. L., Di Achille, G., Komatsu, G., et al. (2022). Geologically recent areas as one key target for identifying active volcanism on Venus. *Geophysical Research Letters*, *49*(22), e2022GL101813. https://doi.org/10.1029/2022gl101813

Djurišić, A. B., Elazar, J. M., & Rakić, A. D. (1997a). Modeling the optical constants of solids using genetic algorithms with parameter space size adjustment. *Optics Communications*, *134*(1–6), 407–414. https://doi.org/10.1016/s0030-4018(96)00546-9

Djurišić, A. B., Elazar, J. M., & Rakić, A. D. (1997b). Simulated-annealing-based genetic algorithm for modeling the optical constants of solids. *Applied Optics*, *36*(28), 7097–7103. https://doi.org/10.1364/ao.36.007097

Donaldson Hanna, K. L., Wyatt, M. B., Thomas, I. R., Bowles, N. E., Greenhagen, B. T., Maturilli, A., et al. (2012). Thermal infrared emissivity measurements under a simulated lunar environment: Application to the Diviner Lunar Radiometer Experiment. *Journal of Geophysical Research*, *117*(E12), E00H05. https://doi.org/10.1029/2011JE003862

Dressler, B., & Reimold, W. (2001). Terrestrial impact melt rocks and glasses. *Earth-Science Reviews*, *56*(1–4), 205–284. https://doi.org/10.1016/s0012-8252(01)00064-2

Dufresne, C. D. M., King, P. L., Dyar, M. D., & Dalby, K. N. (2009). Effect of SiO_2, total FeO, Fe^{3+}/Fe^{2+}, and alkali elements in basaltic glasses on mid-infrared. *American Mineralogist*, *94*(11–12), 1580–1590. https://doi.org/10.2138/am.2009.3113

Dyar, M. D., Gunter, M. E., & Tasa, D. (2008). In *Mineralogy and optical mineralogy*. Mineralogical Society of America Chantilly.

Dyar, M. D., McCanta, M., Breves, E., Carey, C., & Lanzirotti, A. (2016). Accurate predictions of iron redox state in silicate glasses: A multivariate approach using X-ray absorption spectroscopy. *American Mineralogist*, *101*(3), 744–747. https://doi.org/10.2138/am-2016-5555

Dyar, M. D., Ytsma, C., & Lepore, K. (2019). Standards for geochemical analysis of major, minor, and trace elements in rock powders. In *50th annual lunar and planetary science conference*.

Elkins-Tanton, L., Smrekar, S., Hess, P., & Parmentier, E. (2007). Volcanism and volatile recycling on a one-plate planet: Applications to Venus. *Journal of Geophysical Research*, *112*(E4), E04S06. https://doi.org/10.1029/2006je002793

Fisher, R. V., & Schmincke, H.-U. (1984). Alteration of volcanic glass. In *Pyroclastic rocks* (pp. 312–345). Springer Berlin Heidelberg. https://doi.org/10.1007/978-3-642-74864-6_12

Fisher, R. V., & Schmincke, H.-U. (2012). *Pyroclastic rocks*. Springer Science & Business Media.

Formisano, V., Angrilli, F., Arnold, G., Atreya, S., Bianchini, G., Biondi, D., et al. (2005). The Planetary Fourier Spectrometer (PFS) onboard the European Mars express mission. *Planetary and Space Science*, *53*(10), 963–974. https://doi.org/10.1016/j.pss.2004.12.006

Fraser, A. S. (1957). Simulation of genetic systems by automatic digital computers II. Effects of linkage on rates of advance under selection. *Australian Journal of Biological Sciences*, *10*(4), 492–500. https://doi.org/10.1071/bi9570492

Fu, X., Wang, A., & Krawczynski, M. J. (2017). Characterizing amorphous silicates in extraterrestrial materials: Polymerization effects on Raman and mid-IR spectral features of alkali and alkali earth silicate glasses. *Journal of Geophysical Research: Planets*, *122*(5), 839–855. https://doi.org/10.1002/2016JE005241

Garvin, J., Sakimoto, S., Frawley, J., Schnetzler, C., & Wright, H. (2000). Topographic evidence for geologically recent near-polar volcanism on Mars. *Icarus*, *145*(2), 648–652. https://doi.org/10.1006/icar.2000.6409

Glotch, T. D., Bandfield, J. L., Wolff, M. J., Arnold, J. A., & Che, C. (2016). Constraints on the composition and particle size of chloride salt-bearing deposits on Mars. *Journal of Geophysical Research: Planets*, *121*(3), 454–471. https://doi.org/10.1002/2015je004921

Glotch, T. D., & Rossman, G. R. (2009). Mid-infrared reflectance spectra and optical constants of six iron oxide/oxyhydroxide phases. *Icarus*, *204*(2), 663–671. https://doi.org/10.1016/j.icarus.2009.07.024

Glotch, T. D., Rossman, G. R., & Aharonson, O. (2007). Mid-infrared (5–100 μm) reflectance spectra and optical constants of ten phyllosilicate minerals. *Icarus*, *192*(2), 605–622. https://doi.org/10.1016/j.icarus.2007.07.002

Greenhagen, B. T., Lucey, P. G., Wyatt, M. B., Glotch, T. D., Allen, C. C., Arnold, J. A., et al. (2010). Global silicate mineralogy of the Moon from the diviner lunar radiometer. *Science*, *329*(5998), 1507–1509. https://doi.org/10.1126/science.1192196

Grefenstette, J. J. (1993). Genetic algorithms and machine learning. In *Proceedings of the sixth annual conference on computational learning theory*.

Güngör, T., & Saka, B. (2004). Calculation of the optical constants of a thin layer upon a transparent substrate from the reflection spectrum using a genetic algorithm. *Thin Solid Films*, *467*(1–2), 319–325. https://doi.org/10.1016/j.tsf.2004.04.040

Hamilton, V., Christensen, P., Kaplan, H., Haberle, C., Rogers, A., Glotch, T., et al. (2021). Evidence for limited compositional and particle size variation on asteroid (101955) Bennu from thermal infrared spectroscopy. *Astronomy & Astrophysics*, *650*, A120. https://doi.org/10.1051/0004-6361/202039728

Hansen, J. E., & Travis, L. D. (1974). Light scattering in planetary atmospheres. *Space Science Reviews*, *16*(4), 527–610. https://doi.org/10.1007/bf00168069

Haruyama, J., Ohtake, M., Matsunaga, T., Morota, T., Honda, C., Yokota, Y., et al. (2009). Long-lived volcanism on the lunar far-side revealed by SELENE Terrain Camera. *Science*, *323*(5916), 905–908. https://doi.org/10.1126/science.1163382

Hauber, E., Brož, P., Jagert, F., Jodłowski, P., & Platz, T. (2011). Very recent and wide-spread basaltic volcanism on Mars. *Geophysical Research Letters*, *38*(10), L10201. https://doi.org/10.1029/2011gl047310

Head, J. W., Murchie, S. L., Prockter, L. M., Solomon, S. C., Chapman, C. R., Strom, R. G., et al. (2009). Volcanism on Mercury: Evidence from the first MESSENGER flyby for extrusive and explosive activity and the volcanic origin of plains. *Earth and Planetary Science Letters*, *285*(3–4), 227–242. https://doi.org/10.1016/j.epsl.2009.03.007

Head, J. W., & Wilson, L. (1992). Lunar mare volcanism: Stratigraphy, eruption, conditions, and the evolution of secondary crusts. *Geochimica et Cosmochimica Acta*, *56*(6), 2155–2175. https://doi.org/10.1016/0016-7037(92)90183-j

Herrick, R. R., & Hensley, S. (2023). Surface changes observed on a Venusian volcano during the Magellan mission. *Science*, *379*(6638), 1205–1208. https://doi.org/10.1126/science.abm7735

Holland, J. H. (1992). *Adaptation in natural and artificial systems: An introductory analysis with applications to biology, control, and artificial intelligence*. MIT press.

Ito, G., Arnold, J., & Glotch, T. (2017). T-matrix and radiative transfer hybrid models for densely packed particulates at mid-infrared wavelengths. *Journal of Geophysical Research: Planets*, *122*(5), 822–838. https://doi.org/10.1002/2017je005271

Ivanov, M. A., Crumpler, L. S., Aubele, J. C., & Head, J. W., III. (2015). Volcanism on Venus. In *The encyclopedia of volcanoes* (pp. 729–746). Elsevier.

Ivanovski, V., Mayerhöfer, T. G., Popp, J., & Petruševski, V. M. (2008). Polarized IR reflectance spectra of the monoclinic single crystal $K_2Ni(SO_4)_2 \cdot 6H_2O$: Dispersion analysis, dielectric and optical properties. *Spectrochimica Acta Part A: Molecular and Biomolecular Spectroscopy*, *69*(2), 629–641. https://doi.org/10.1016/j.saa.2007.05.014

Jaret, S. J., Johnson, J. R., Sims, M., DiFrancesco, N., & Glotch, T. D. (2018). Microspectroscopic and petrographic comparison of experimentally shocked albite, andesine, and bytownite. *Journal of Geophysical Research: Planets*, *123*(7), 1701–1722. https://doi.org/10.1029/2018je005523

Jaret, S. J., Woerner, W. R., Phillips, B. L., Ehm, L., Nekvasil, H., Wright, S. P., & Glotch, T. D. (2015). Maskelynite formation via solid-state transformation: Evidence of infrared and X-ray anisotropy. *Journal of Geophysical Research: Planets*, *120*(3), 570–587. https://doi.org/10.1002/2014je004764

Johnson, J. R., Jaret, S. J., Glotch, T. D., & Sims, M. (2020). Raman and infrared microspectroscopy of experimentally shocked basalts. *Journal of Geophysical Research: Planets*, *125*(2), e2019JE006240. https://doi.org/10.1029/2019je006240

Jozwiak, L. M., Head, J. W., & Wilson, L. (2018). Explosive volcanism on Mercury: Analysis of vent and deposit morphology and modes of eruption. *Icarus*, *302*, 191–212. https://doi.org/10.1016/j.icarus.2017.11.011

Kerber, L., Head, J. W., Blewett, D. T., Solomon, S. C., Wilson, L., Murchie, S. L., et al. (2011). The global distribution of pyroclastic deposits on Mercury: The view from MESSENGER flybys 1–3. *Planetary and Space Science*, *59*(15), 1895–1909. https://doi.org/10.1016/j.pss.2011.03.020

Kerber, L., Head, J. W., Solomon, S. C., Murchie, S. L., Blewett, D. T., & Wilson, L. (2009). Explosive volcanic eruptions on Mercury: Eruption conditions, magma volatile content, and implications for interior volatile abundances. *Earth and Planetary Science Letters*, *285*(3–4), 263–271. https://doi.org/10.1016/j.epsl.2009.04.037

King, P. L., & Larsen, J. F. (2013). A micro-reflectance IR spectroscopy method for analyzing volatile species in basaltic, andesitic, phonolitic, and rhyolitic glasses. *American Mineralogist*, *98*(7), 1162–1171. https://doi.org/10.2138/am.2013.4277

King, P. L., Ramsey, M. S., & Swayze, G. A. (2004). *Infrared spectroscopy in geochemistry, exploration geochemistry and remote sensing* (Vol. 33). Mineralogical Association of Canada.

Koohestani, B. (2020). A crossover operator for improving the efficiency of permutation-based genetic algorithms. *Expert Systems with Applications*, *151*, 113381. https://doi.org/10.1016/j.eswa.2020.113381

Leight, C. J., McCanta, M. C., Glotch, T. D., Thomson, B. J., Ye, C., & Dyar, M. D. (2022). Characterization of tephra deposits using VNIR and MIR spectroscopy: A comprehensive terrestrial tephra spectral library. *Remote Sensing of Environment*, *273*, 112965. https://doi.org/10.1016/j.rse.2022.112965

Long, T., Qian, Y., Norman, M. D., Miljkovic, K., Crow, C., Head, J. W., et al. (2022). Constraining the formation and transport of lunar impact glasses using the ages and chemical compositions of Chang'E-5 glass beads. *Science Advances*, *8*(39), eabq2542. https://doi.org/10.1126/sciadv.abq2542

Marsili Libelli, S., & Alba, P. (2000). Adaptive mutation in genetic algorithms. *Soft Computing*, *4*(2), 76–80. https://doi.org/10.1007/s005000000042

McEwen, A. S., Malin, M. C., Carr, M. H., & Hartmann, W. K. (1999). Voluminous volcanism on early Mars revealed in Valles Marineris. *Nature*, *397*(6720), 584–586. https://doi.org/10.1038/17539

Minitti, M. E., & Hamilton, V. E. (2010). A search for basaltic-to-intermediate glasses on Mars: Assessing Martian crustal mineralogy. *Icarus*, *210*(1), 135–149. https://doi.org/10.1016/j.icarus.2010.06.028

Mocioiu, O. C., Popa, M., Neacsu, E. I., & Zaharescu, M. (2013). Correlation of structural units and chemical stability in SiO_2–PbO–Na_2O ternary glasses: Spectroscopic methods. *Journal of Non-Crystalline Solids*, *361*, 130–141. https://doi.org/10.1016/j.jnoncrysol.2012.10.015

Mooney, T., & Knacke, R. (1985). Optical constants of chlorite and serpentine between 2.5 and 50 μm. *Icarus*, *64*(3), 493–502. https://doi.org/10.1016/0019-1035(85)90070-3

Morlok, A., Renggli, C., Charlier, B., Reitze, M. P., Klemme, S., Namur, O., et al. (2021). Mid-infrared reflectance spectroscopy of synthetic glass analogs for Mercury surface studies. *Icarus*, *361*, 114363. https://doi.org/10.1016/j.icarus.2021.114363

Moroz, L., Basilevsky, A., Hiroi, T., Rout, S., Baither, D., Van Der Bogert, C., et al. (2009). Spectral properties of simulated impact glasses produced from Martian soil analogue JSC Mars-1. *Icarus*, *202*(1), 336–353. https://doi.org/10.1016/j.icarus.2009.02.007

Nimmo, F., & McKenzie, D. (1998). Volcanism and tectonics on Venus. *Annual Review of Earth and Planetary Sciences*, *26*(1), 23–51. https://doi.org/10.1146/annurev.earth.26.1.23

Nocuń, M., & Handke, M. (2001). Structural inhomogeneity in glasses from the system Li_2O_3–Al_2O_3–SiO_2 revealed by IR spectroscopy. *Journal of Molecular Structure*, *596*(1), 139–143. https://doi.org/10.1016/S0022-2860(01)00701-3

Onari, S., Arai, T., & Kudo, K. (1977). Infrared lattice vibrations and dielectric dispersion in $\alpha-$ Fe_2O_3. *Physical Review B*, *16*(4), 1717–1721. https://doi.org/10.1103/physrevb.16.1717

Paige, D., Foote, M., Greenhagen, B., Schofield, J., Calcutt, S., Vasavada, A., et al. (2010). The lunar reconnaissance orbiter diviner lunar radiometer experiment. *Space Science Reviews*, *150*(1), 125–160. https://doi.org/10.1007/s11214-009-9529-2

Patrick, R. R., & Howe, R. C. (1994). Volcanism on the terrestrial planets. *Journal of Geological Education*, *42*(3), 225–238. https://doi.org/10.5408/0022-1368-42.3.225

Pieters, C. M., Fischer, E. M., Rode, O., & Basu, A. (1993). Optical effects of space weathering: The role of the finest fraction. *Journal of Geophysical Research*, *98*(E11), 20817–20824. https://doi.org/10.1029/93je02467

Pieters, C. M., Head, J. W., Gaddis, L., Jolliff, B., & Duke, M. (2001). Rock types of South Pole-Aitken basin and extent of basaltic volcanism. *Journal of Geophysical Research*, *106*(E11), 28001–28022. https://doi.org/10.1029/2000je001414

Pollack, J. B., Toon, O. B., & Khare, B. N. (1973). Optical properties of some terrestrial rocks and glasses. *Icarus*, *19*(3), 372–389. https://doi.org/10.1016/0019-1035(73)90115-2

Querry, M. R., Osborne, G., Lies, K., Jordon, R., & Coveney, R. M. (1978). Complex refractive index of limestone in the visible and infrared. *Applied Optics*, *17*(3), 353–356. https://doi.org/10.1364/ao.17.000353

Rhodes, J., & Vollinger, M. (2004). Composition of basaltic lavas sampled by phase-2 of the Hawaii Scientific Drilling Project: Geochemical stratigraphy and magma types. *Geochemistry, Geophysics, Geosystems*, *5*(3), Q03G13. https://doi.org/10.1029/2002gc000434

Roush, T., Pollack, J., & Orenberg, J. (1991). Derivation of midinfrared (5–25 μm) optical constants of some silicates and palagonite. *Icarus*, *94*(1), 191–208. https://doi.org/10.1016/0019-1035(91)90150-r

Rucks, M. J., Ye, C., Sklute, E. C., Arnold, J. A., DiFrancesco, N. J., & Glotch, T. D. (2022). Visible to mid-infrared optical constants of Orthopyroxenes. *Earth and Space Science*, *9*(4), e2021EA002104. https://doi.org/10.1029/2021ea002104

Saal, A. E., Hauri, E. H., Cascio, M. L., Van Orman, J. A., Rutherford, M. C., & Cooper, R. F. (2008). Volatile content of lunar volcanic glasses and the presence of water in the Moon's interior. *Nature*, *454*(7201), 192–195. https://doi.org/10.1038/nature07047

Saal, A. E., Hauri, E. H., Van Orman, J. A., & Rutherford, M. J. (2013). Hydrogen isotopes in lunar volcanic glasses and melt inclusions reveal a carbonaceous chondrite heritage. *Science*, *340*(6138), 1317–1320. https://doi.org/10.1126/science.1235142

Salisbury, J. W., D'Aria, D. M., & Jarosewich, E. (1991). Midinfrared (2.5–13.5 μm) reflectance spectra of powdered stony meteorites. *Icarus*, *92*(2), 280–297. https://doi.org/10.1016/0019-1035(91)90052-U

Salisbury, J. W., & Wald, A. (1992). The role of volume scattering in reducing spectral contrast of reststrahlen bands in spectra of powdered minerals. *Icarus*, *96*(1), 121–128. https://doi.org/10.1016/0019-1035(92)90009-v

Schafer, R. W. (2011). What is a Savitzky-Golay filter? [Lecture notes]. *IEEE Signal Processing Magazine*, *28*(4), 111–117. https://doi.org/10.1109/MSP.2011.941097

Schultz, P. H., & Spudis, P. D. (1983). Beginning and end of lunar mare volcanism. *Nature*, *302*(5905), 233–236. https://doi.org/10.1038/302233a0

Sheta, A. F., & De Jong, K. (1996). Parameter estimation of nonlinear systems in noisy environments using genetic algorithms. In *Proceedings of the 1996 IEEE international symposium on intelligent control*.

Silverman, S., Peralta, R., Christensen, P., & Mehall, G. (2006). Miniature thermal emission spectrometer for the Mars exploration rover. *Acta Astronautica*, *59*(8), 990–999. https://doi.org/10.1016/j.actaastro.2005.07.055

Sklute, E. C., Glotch, T. D., Piatek, J. L., Woerner, W. R., Martone, A. A., & Kraner, M. L. (2015). Optical constants of synthetic potassium, sodium, and hydronium jarosite. *American Mineralogist*, *100*(5–6), 1110–1122. https://doi.org/10.2138/am-2015-4824

Smrekar, S. E., Stofan, E. R., Mueller, N., Treiman, A., Elkins-Tanton, L., Helbert, J., et al. (2010). Recent hotspot volcanism on Venus from VIRTIS emissivity data. *Science*, *328*(5978), 605–608. https://doi.org/10.1126/science.1186785

Speck, A. K., Whittington, A. G., & Hofmeister, A. M. (2011). Disordered silicates in space: A study of laboratory spectra of "amorphous" silicates. *The Astrophysical Journal*, *740*(2), 93. https://doi.org/10.1088/0004-637X/740/2/93

Spitzer, W., & Kleinman, D. (1961). Infrared lattice bands of quartz. *Physical Review*, *121*(5), 1324–1335. https://doi.org/10.1103/physrev.121.1324

Stoch, L., & Środa, M. (1999). Infrared spectroscopy in the investigation of oxide glasses structure. *Journal of Molecular Structure*, *511–512*, 77–84. https://doi.org/10.1016/S0022-2860(99)00146-5

Stöffler, D. (1984). Glasses formed by hypervelocity impact. *Journal of Non-Crystalline Solids*, *67*(1), 465–502. https://doi.org/10.1016/0022-3093(84)90171-6

Thomas, R. J., Rothery, D. A., Conway, S. J., & Anand, M. (2014). Long-lived explosive volcanism on Mercury. *Geophysical Research Letters*, *41*(17), 6084–6092. https://doi.org/10.1002/2014gl061224

Tomassini, M. (1995). A survey of genetic algorithms. *Annual reviews of computational physics*, *III*, 87–118.

Tompkins, S., & Pieters, C. M. (2010). Spectral characteristics of lunar impact melts and inferred mineralogy. *Meteoritics & Planetary Sciences*, *45*(7), 1152–1169. https://doi.org/10.1111/j.1945-5100.2010.01074.x

Toon, O. B., Pollack, J. B., & Sagan, C. (1977). Physical properties of the particles composing the Martian dust storm of 1971–1972. *Icarus*, *30*(4), 663–696. https://doi.org/10.1016/0019-1035(77)90088-4

Torres-Costa, V., Martín-Palma, R., & Martínez-Duart, J. (2004). Optical constants of porous silicon films and multilayers determined by genetic algorithms. *Journal of Applied Physics*, *96*(8), 4197–4203. https://doi.org/10.1063/1.1786672

Varatharajan, I., Sklute, E., Glotch, T. D., & Dyar, M. D. (2023a). Mid-infrared optical constants of silicate glasses supporting planetary surface science and spectroscopy studies [Sofware]. Github. Retrieved from https://github.com/astroindhu/Genetic-Algorithm-for-MIR-optical-constants-modeling

Varatharajan, I., Sklute, E., Glotch, T. D., & Dyar, M. D. (2023b). Mid-infrared optical constants of silicate glasses supporting planetary surface science and spectroscopy studies [Dataset]. Zenodo. https://doi.org/10.5281/zenodo.7713109

Weider, S. Z., Nittler, L. R., Murchie, S. L., Peplowski, P. N., McCoy, T. J., Kerber, L., et al. (2016). Evidence from MESSENGER for sulfur- and carbon-driven explosive volcanism on Mercury. *Geophysical Research Letters*, *43*(8), 3653–3661. https://doi.org/10.1002/2016gl068325

Wilson, L., & Head, J. W. (1981). Ascent and eruption of basaltic magma on the Earth and Moon. *Journal of Geophysical Research*, *86*(B4), 2971–3001. https://doi.org/10.1029/jb086ib04p02971

Ye, C., Rucks, M. J., Arnold, J. A., & Glotch, T. D. (2019). Mid-infrared optical constants of labradorite, a triclinic plagioclase mineral. *Earth and Space Science*, *6*(12), 2410–2422. https://doi.org/10.1029/2019ea000915

Ye, C., Sklute, E. C., & Glotch, T. D. (2021). Orientation averaged visible/near-infrared and mid-infrared optical constants of hydrous Ca-sulfates: Gypsum and Bassanite. *Earth and Space Science*, *8*(10), e2021EA001834. https://doi.org/10.1029/2021ea001834

Zellner, N. (2019). Lunar impact glasses: Probing the Moon's surface and constraining its impact history. *Journal of Geophysical Research: Planets*, *124*(11), 2686–2702. https://doi.org/10.1029/2019je006050

Zimbelman, J. R., Garry, W. B., Bleacher, J. E., & Crown, D. A. (2015). Volcanism on Mars. In *The Encyclopedia of volcanoes* (pp. 717–728). Elsevier.